 CMES, vol.21, no.2, pp.105-132, 2007

Slow Viscous Migration of a Conducting Solid Particle under the Action of Uniform Ambient Electric and Magnetic Fields

A. Sellier[1]

Abstract: We examine the low-Reynolds-number migration of a conducting and arbitrarily-shaped solid particle freely immersed in a metal liquid of different conductivity when subject to uniform ambient electric and magnetic fields. The boundary formulation established elsewhere for an insulating particle is extended and the incurred particle's rigid-body motion is then obtained by determinating a very few surface quantities on the particle's surface. The behavior of either oblate or prolate conducting spheroids is analytically investigated and the poposed procedure for the challenging case of other non-trivial geometries is implemented and benchmarked against those solutions. The numerical implementation makes it possible to obtain the rigid-body motion of conducting tori and pear-shaped particles. If the conducting torus does not rotate (since orthotropic) and, depending on its shape, is seen to translate like an oblate or a prolate spheroid the pear-shaped particles are by contrast found to translate and rotate therefore experiencing a time-dependent migration. In addition, the rigid-body motion of conducting tori and pear-shaped particles strongly depends not nonly upon the particle's shape and conductivity ratio but also upon the external electric and magnetic fields.

Keyword: MagnetoHydrodynamics, Stokes flow, conducting particle, boundary-integral equations.

1 Introduction

As first predicted by Kolin (1953), Leenov and Kolin (1954) and experimentally confirmed by Marty and Alemany (1984), a conducting or insulating solid particle freely suspended in a liquid metal of different conductivity moves when subject to uniform ambient electric and magnetic fields $\mathbf{E}$ and $\mathbf{B}$. Due to the resulting Lorentz body force, the metal of uniform conductivity $\sigma > 0$ indeed experiences a viscous flow which, by viscosity, makes the particle of constant conductivity $\sigma_s \geq 0$ migrate as soon as $\sigma_s \neq \sigma$. Since this phenomenon may receive applications in impurities removal, it is of interest to determine the incurred rigid-body motion of the particle, i. e. its translational and angular velocities $\mathbf{U}$ and $\boldsymbol{\omega}$. Such quantities depend upon the particle shape and conductivity σ_s, the liquid metal uniform kinematic viscosity μ and conductivity σ and the uniform ambient electric field $\mathbf{E}$ and magnetic field $\mathbf{B}$. The simple case of conducting spheres and cylinders has been addressed by Leenov and Kolin (1954) and Marty and Alemany (1984) but solid impurities may adopt other shapes. Thus, Moffatt and Sellier (2002) and Sellier (2003a) recently considered non-spherical particles. In Moffatt and Sellier (2002) a general theory is proposed for an arbitrarily-shaped insulating particle ($\sigma_s = 0$) and both $\mathbf{U}$ and $\boldsymbol{\omega}$ are shown to be bilinear in $\mathbf{E}$ and $\mathbf{B}$. Appealing to symmetry properties, such relationships are found to depend upon a very few shape-sensitive coefficients for isotropic, axisymmetric and orthotropic insulating particles. In order to calculate such unknown coefficients and to deal with a general geometry, Sellier (2003a) proposed a boundary formulation to determine $(\mathbf{U}, \boldsymbol{\omega})$ for an arbitrarily-shaped but nonconductive particle and analytically worked out the advocated procedure for insulating ellipsoids.

The present work addresses the challenging case of either conducting or insulating ($\sigma_s \geq 0$) and arbitrarily-shaped particles within the physical framework introduced in Moffatt and Sellier (2002). It is actually straightforward to extend the

[1] LadHyX, Ecole Polytechnique, FRANCE

results and conclusions of this latter paper to the case of a conducting particle and the arguments will not be repeated here (for example, any conducting and orthotropic particle does not rotate and if isotropic translates parallel to $\mathbf{E}\wedge\mathbf{B}$). However, in any case the evaluation of $(\mathbf{U},\boldsymbol{\omega})$ requires further investigations and this study both presents and implements a suitable numerical strategy to calculate, at a reasonable cost, the rigid-body motion of an arbitrary conducting particle.

The paper is organized as follows. In §2 we give the key linear system that governs the unknown cartesian velocity components of the solid body and show how to calculate the migration from the knowledge of a very few quantities on the surface of the particle. The motion of a conducting ellipsoid is then analytically obtained and thoroughly discussed in §3. Relevant boundary-integral equations, that provide the previously alluded to key surface quantities, are given in §4 whereas §5 both presents the numerical implementation of the whole proposed procedure and discusses a few carefully-selected illustrating examples: the benchmark problem of the conducting ellipsoid, the case of a conducting torus and finally the challenging case of a conducting pear-shaped particle. Finally, a few concluding remarks close the paper in §6.

2 Governing equations

This section reduces the determination of the rigid-body motion of any conducting particle to the evaluation of a few quantities on its surface. For a sake of conciseness, the reader is whenever possible directed to the material available in Moffatt and Sellier (2002) or Sellier (2003a).

2.1 The governing system for the particle's rigid-body motion

This subsection briefly introduces our problem and the key linar system that governs the unknown translational and angular velocities of the particle. As sketched in figure 1, this latter is a solid $\mathscr{P}$, of uniform conductivity $\sigma_s \geq 0$ and smooth enough surface S, freely immersed in a Newtonian liquid metal of uniform density ρ, kinematic viscosity μ and conductivity $\sigma > 0$ occupying the unbounded domain Ω. Cartesian coordinates (O,x_1,x_2,x_3) centered at one point O attached to the particle are adopted with $\mathbf{x} = \mathbf{OM}, x_i = \mathbf{x}.\mathbf{e}_i$ and $r = |\mathbf{x}|$.

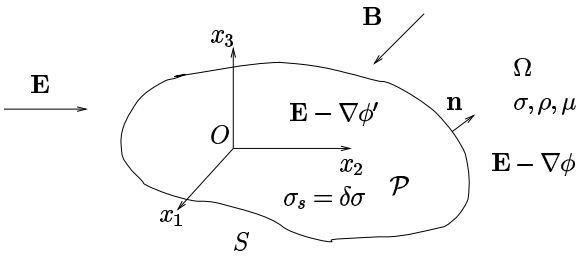

Figure 1: A conducting particle subject to uniform ambient electric and magnetic fields **E** and **B**.

Far from $\mathscr{P}$, steady uniform ambient electric and magnetic fields **E** and **B** are separately and externally applied. The particle does not modify the magnetic field (Moffatt and Sellier (2002)) but whenever its conductivity differs from the liquid conductivity it perturbs **E** to $\mathbf{E}-\nabla\phi'$ in $\mathscr{P}$ and $\mathbf{E}-\nabla\phi$ in Ω if ϕ' and ϕ designate the harmonic perturbation electrostatic potentials inside and outside the particle, respectively. In Ω the resulting non-uniform current **j** and rotational Lorentz body force $\mathbf{j}\wedge\mathbf{B}$ induce a quasi-steady flow of velocity **u** and pressure p and by viscosity a rigid-body motion $(\mathbf{U},\boldsymbol{\omega})$ of $\mathscr{P}$, with **U** the velocity of the point O attached to $\mathscr{P}$. If $\mathscr{P}$ has length scale a of order 1mm or less the fluid velocity scale U is of order $\sigma|\mathbf{E}||\mathbf{B}|a^2/\mu$ and both the Reynolds number $\mathrm{Re} = \rho U a/\mu$ and Hartmann number $M = |\mathbf{B}|a(\sigma/\mu)^{1/2}$ are small (Moffatt and Sellier (2002)). From $M \ll 1$ one obtains

$$\mathbf{j} = \sigma(\mathbf{E}-\nabla\phi+\mathbf{u}\wedge\mathbf{B}) \sim \sigma(\mathbf{E}-\nabla\phi) \text{ in } \Omega, \quad (1)$$

whereas the induced current in the solid particle becomes $\mathbf{j}' = \sigma_s(\mathbf{E}-\nabla\phi')$. Exploiting (1) and requiring the continuity of the normal current and tangential perturbed electric field across the particle surface Jackson (1975), we thus arrive at the following well-posed governing problem for

ϕ and ϕ'

$$\begin{aligned}\nabla^2\phi' &= 0 \text{ in } \mathscr{P},\\ \nabla^2\phi &= 0 \text{ in } \Omega,\\ \nabla\phi &\to \mathbf{0} \text{ as } r\to\infty,\end{aligned} \tag{2}$$

$$\sigma_s(\mathbf{E}-\nabla\phi').\mathbf{n} = \sigma(\mathbf{E}-\nabla\phi).\mathbf{n} \text{ on } S \tag{3}$$

$$(\mathbf{E}-\nabla\phi')\wedge\mathbf{n} = (\mathbf{E}-\nabla\phi)\wedge\mathbf{n} \text{ on } S \tag{4}$$

where $\mathbf{n}$ denotes the unit outward normal on S. Solving (2)-(4) provides the potentials ϕ' and ϕ, in $\mathscr{P}$ and Ω respectively, independently of the fluid motion $(\mathbf{u},p)$. Under the assumption $\mathrm{Re}\ll 1$, this flow fulfills the steady Stokes equations (Sellier (2003a))

$$\nabla.\mathbf{u} = 0 \text{ and } \mu\nabla^2\mathbf{u} = \nabla p - \mathbf{f} \text{ in } \Omega, \tag{5}$$

$$(\mathbf{u},p)\to(\mathbf{0},p_\infty) \text{ as } r\to\infty,\ \mathbf{u}=\mathbf{u}_d \text{ on } S \tag{6}$$

for the approximated Lorentz body force $\mathbf{f} = \sigma(\mathbf{E}-\nabla\phi)\wedge\mathbf{B}$, the far-field pressure $p_\infty = (\sigma\mathbf{E}\wedge\mathbf{B}).\mathbf{x}$ and the prescribed rigid-body velocity $\mathbf{u}_d = \mathbf{U}+\boldsymbol{\omega}\wedge\mathbf{x}$.

The net force $\mathbf{F}'$ and torque $\mathbf{G}'$ (with respect to O) exerted on the solid particle by the Lorentz body force $\mathbf{j}'\wedge\mathbf{B}$ inside $\mathscr{P}$ readily read

$$\mathbf{F}' = \sigma_s\left[\int_{\mathscr{P}}(\mathbf{E}-\nabla\phi')dv\right]\wedge\mathbf{B}, \tag{7}$$

$$\mathbf{G}' = \sigma_s\int_{\mathscr{P}}\mathbf{x}\wedge\left[(\mathbf{E}-\nabla\phi')\wedge\mathbf{B}\right]dv. \tag{8}$$

The metal flow $(\mathbf{u},p)$, subject to (5)-(6), also applies on the particle a net force $\mathbf{F}$ and a net torque $\mathbf{G}$ (with respect to O) whose determination in terms of $(\mathbf{U},\boldsymbol{\omega})$ requires the prerequisite obtention of ϕ. As recalled in §2.2, this potential actually admits a $1/r^2-$decay far from S. This 'good' far-field behavior permits us to express $\mathbf{F}$ and $\mathbf{G}$ as achieved in Sellier Sellier (2003a) by introducing six widely-employed (Happel and Brenner (1973)) steady Stokes flows $(\mathbf{u}_T^{(i)},p_T^{(i)})$ and $(\mathbf{u}_R^{(i)},p_R^{(i)})$ of the metal for $i=1,2,3$. These specific flows which are free from body forces, quiescent far from S and associated to pure translations or rotations of $\mathscr{P}$ with the boundary conditions $\mathbf{u}_T^{(i)}=\mathbf{e}_i$ and $\mathbf{u}_R^{(i)}=\mathbf{e}_i\wedge\mathbf{x}$ on the particle surface, induce the surface force densities $\mathbf{f}_T^{(i)}$ and $\mathbf{f}_R^{(i)}$ on S. Adopting henceforth the usual tensor summation convention such that, for instance, $\mathbf{v}=v_i\mathbf{e}_i$ and $\mathbf{T}=T_{ij}\mathbf{e}_i\otimes\mathbf{e}_j$ for a vector $\mathbf{v}$ and a second-rank tensor $\mathbf{T}$ of Cartesian components v_i and T_{ij}, the net force and torque $\mathbf{F}$ and $\mathbf{G}$ are found to be (Sellier (2003a))

$$\begin{aligned}\mathbf{F} = -\mu\{\mathbf{K}.\mathbf{U}+\mathbf{V}.\boldsymbol{\omega}\} - \sigma\mathscr{V}_{\mathscr{P}}[\mathbf{E}\wedge\mathbf{B}]\\ -\sigma\left(\int_\Omega\mathbf{u}_T^{(i)}.[\nabla\phi\wedge\mathbf{B}]dv\right)\mathbf{e}_i,\end{aligned} \tag{9}$$

$$\begin{aligned}\mathbf{G} = -\mu\{\mathbf{D}.\mathbf{U}+\mathbf{W}.\boldsymbol{\omega}\} + \sigma[\mathbf{E}\wedge\mathbf{B}]\wedge\left[\int_{\mathscr{P}}\mathbf{x}dv\right]\\ -\sigma\left(\int_\Omega\mathbf{u}_R^{(i)}.[\nabla\phi\wedge\mathbf{B}]dv\right)\mathbf{e}_i,\end{aligned} \tag{10}$$

where $\mathscr{V}_{\mathscr{P}}$ denotes the volume of $\mathscr{P}$ and the first term on the right-hand side of (7) or (8) is readily the net force or torque acting on the particle when it moves at the velocities $\mathbf{U}$ and $\boldsymbol{\omega}$ in absence of any electromagnetic body force. In other words, the occurring second-rank tensors $\mathbf{K},\mathbf{W},\mathbf{V}$ and $\mathbf{D}$ are the standard (Kim and Karrila (1991)) translation, rotation tensors with Cartesian components

$$-\mu K_{ij} = \int_S\mathbf{e}_j.\mathbf{f}_T^{(i)}dS,\ -\mu W_{ij} = \int_S[\mathbf{e}_j\wedge\mathbf{x}].\mathbf{f}_R^{(i)}dS, \tag{11}$$

$$-\mu V_{ij} = \int_S[\mathbf{e}_j\wedge\mathbf{x}].\mathbf{f}_T^{(i)}dS,\ -\mu D_{ij} = \int_S\mathbf{e}_j.\mathbf{f}_R^{(i)}dS. \tag{12}$$

At this stage, one should note that both $\mathbf{f}_T^{(i)}$ and $\mathbf{f}_R^{(i)}$ are defined up to a constant multiple of the unit normal $\mathbf{n}$ (since one may add any constant to the fluid pressure, Ladyzhenskaya (1969)). However, adding $\lambda\mathbf{n}$ to $\mathbf{f}_T^{(i)}$ and $\mathbf{f}_R^{(i)}$ with λ constant does not change the previous tensors Cartesian components nor $\mathbf{F}$ or $\mathbf{G}$. Since the particle is freely suspended we have $\mathbf{F}+\mathbf{F}'=\mathbf{0}$ and $\mathbf{G}+\mathbf{G}'=\mathbf{0}$. By virtue of (6) and (9)-(10), one accordingly obtains the coupled equations

$$\begin{aligned}\mathbf{K}.\mathbf{U}+\mathbf{V}.\boldsymbol{\omega} = \frac{\sigma}{\mu}\Bigg\{(\delta-1)\mathscr{V}_{\mathscr{P}}\mathbf{E}\wedge\mathbf{B}\\ -\left(\int_\Omega\mathbf{u}_T^{(i)}.[\nabla\phi\wedge\mathbf{B}]dv\right)\mathbf{e}_i-\delta\left[\int_{\mathscr{P}}\nabla\phi'dv\right]\wedge\mathbf{B}\Bigg\},\end{aligned} \tag{13}$$

$$\mathbf{D}.\mathbf{U}+\mathbf{W}.\boldsymbol{\omega}=\frac{\sigma}{\mu}\left\{(\delta-1)\left[\int_{\mathscr{P}}\mathbf{x}dv\right]\wedge[\mathbf{E}\wedge\mathbf{B}]\right.$$
$$\left.-\left(\int_{\Omega}\mathbf{u}_R^{(i)}.[\nabla\phi\wedge\mathbf{B}]dv\right)\mathbf{e}_i-\delta\int_{\mathscr{P}}\mathbf{x}\wedge[\nabla\phi'\wedge\mathbf{B}]dv\right\} \tag{14}$$

where $\delta=\sigma_s/\sigma\geq 0$ denotes the particle's conductivity ratio. By virtue of (11)-(12), the linear system (13)-(14) admits a 6×6 symmetric and positive-definite matrix (Happel and Brenner (1973)) and thus a unique solution $(\mathbf{U},\boldsymbol{\omega})$.

2.2 Needed surface quantities

Inspecting (11)-(14) suggests that the evaluation of $(\mathbf{U},\boldsymbol{\omega})$ requires to calculate the surface forces $\mathbf{f}_T^{(i)}$ and $\mathbf{f}_R^{(i)}$ on S but also the vectors $\mathbf{u}_T^{(i)},\mathbf{u}_R^{(i)},\nabla\phi$ in Ω and $\nabla\phi'$ in $\mathscr{P}$. This subsection shows how one may however content oneself with the knowledge of $\mathbf{f}_T^{(i)},\mathbf{f}_R^{(i)}$ and a few quantities on the surface S to obtain the particle rigid-body motion. The first step in this direction has been achieved in Sellier (2003a) where it is established that, under the 'good' far-field $1/r^2-$decay of ϕ,

$$\int_{\Omega}\mathbf{u}_L^{(i)}.[\nabla\phi\wedge\mathbf{B}]dv=-\frac{\sigma}{8\pi\mu}$$
$$\times\int_S\int_S\left\{\varepsilon_{kmn}PM\left[\mathbf{f}_L^{(i)}.\mathbf{e}_k\right](P)[\mathbf{B}.\mathbf{e}_n]\left[\nabla(\phi_{,m}).\mathbf{n}\right](M)\right.$$
$$+\left[\mathbf{f}_L^{(i)}(P).\frac{\mathbf{PM}}{PM}\right]\left[\nabla\phi(M)\wedge\mathbf{B}\right].\mathbf{n}(M)$$
$$\left.-\mathbf{f}_L^{(i)}(P).[\nabla\phi(M)\wedge\mathbf{B}]\frac{\mathbf{PM}.\mathbf{n}(M)}{PM}\right\}dS_PdS_M, \tag{15}$$

if $L\in\{T,R\}$ and $\varepsilon_{kmn}\mathbf{e}_k\otimes\mathbf{e}_m\otimes\mathbf{e}_n$ designates the usual third-rank antisymmetric permutation tensor. In order to treat the first and third terms occurring on the right-hand sides of (11)-(12), let us introduce the unknown polarization surface-charge density q induced (Jackson (1975)) by the ambient electric field $\mathbf{E}$ on S. The potentials ϕ' and ϕ, subject to (2)-(4), then adopt the single-layer representations

$$\phi'=\psi \text{ in } \mathscr{P},\ \phi=\psi \text{ in } \Omega,\ \psi(M)=\int_S\frac{q(P)dS_P}{4\pi PM}. \tag{16}$$

Note that (16) both ensures (2) and $\phi'=\phi$ on S, i. e. the boundary condition (4). In addition, (16) and the condition (3) immediately yield

$$q=(\nabla\phi'-\nabla\phi).\mathbf{n} \text{ on } S, \tag{17}$$
$$(\delta-1)\mathbf{E}.\mathbf{n}=(\delta-1)\nabla\phi'.\mathbf{n}+q \text{ on } S. \tag{18}$$

As detailed in Appendix A, the net polarization charge on S is thus zero, i.e. the particle is electrically neutral. This property ensures the announced 'good' $1/r^2-$decay of ϕ far from the particle. The obtention of the arising surface-charge density q from the combination of (18) and the representation (16) is postponed to §4. Exploiting the relation (16) in the particle, the previous continuity of the perturbation potential across its surface S and using the divergence theorem, we not only obtain the useful identities

$$\mathscr{V}_{\mathscr{P}}=\int_S\left(\frac{\mathbf{x}}{3}\right).\mathbf{n}dS,$$
$$\int_{\mathscr{P}}\mathbf{x}dv=\sum_{i=1}^{3}\left[\int_S\left(\frac{x_i^2}{2}\right)\mathbf{e}_i.\mathbf{n}dS\right]\mathbf{e}_i, \tag{19}$$

$$\int_{\mathscr{P}}\nabla\phi'dv=\left[\int_S\phi(\mathbf{x})\mathbf{e}_i.\mathbf{n}dS\right]\mathbf{e}_i \tag{20}$$

but also the key relation, established in Appendix A,

$$\int_{\mathscr{P}}\mathbf{x}\wedge[\nabla\phi'\wedge\mathbf{B}]dv=\sum_{i=1}^{3}\left[\int_S\left\{q(\mathbf{x})h(\mathbf{x})\mathbf{B}.\mathbf{e}_i\right.\right.$$
$$\left.\left.+\phi(\mathbf{x})\left[(\mathbf{B}.\mathbf{x})\mathbf{e}_i-(\mathbf{B}.\mathbf{e}_i)\mathbf{x}\right].\mathbf{n}\right\}dS\right]\mathbf{e}_i, \tag{21}$$

$$h(\mathbf{x})=\int_S\frac{\mathbf{MP}.\mathbf{n}(P)}{4\pi MP}dS_P \text{ for } \mathbf{x}=\mathbf{OM} \text{ on } S. \tag{22}$$

In summary, the relations (11)-(15) and (20)-(22) clearly show that the determination of the rigid-body motion $(\mathbf{U},\boldsymbol{\omega})$ of a conducting particle only requires to evaluate on its surface S the surface forces $\mathbf{f}_T^{(i)},\mathbf{f}_R^{(i)}$, the polarization charge density q and also the perturbation potential ϕ together with its gradient $\nabla\phi=\phi_{,m}\mathbf{e}_m$ and normal fluxes $\nabla(\phi_{,m}).\mathbf{n}$. Note that one should first obtain the density q since, by virtue of (3) and (17)-(18), the function ϕ obeys the well-posed exterior Neumann problem

$$\nabla^2\phi=0 \text{ in } \Omega \text{ and } r\phi\to 0 \text{ as } r\to\infty \tag{23}$$

$$\nabla\phi.\mathbf{n} = \mathbf{E}.\mathbf{n} - \frac{\delta q}{\delta - 1} \text{ on } S. \tag{24}$$

Before presenting a suitable numerical strategy to calculate the previous surface quantities and thereby the rigid-body motion $(\mathbf{U}, \boldsymbol{\omega})$ of an arbitrarily-shaped conducting particle in §4, it is worth working out analytically a benchmark problem for a simple geometry. This is achieved in §3 for ellipsoidal particles.

3 Translation of a conducting ellipsoid

As pointed out in the introduction, it is straightforward to extend the conclusions of Moffatt and Sellier (2002) to the case of a conducting particle of non-zero relative conductivity $\delta = \sigma_s/\sigma$. As a consequence, any conducting orthotropic solid that has three orthogonal planes of symmetry intersecting at its centre of volume O and normal to vectors $\mathbf{e}_i$ is found to experience a rigid-body motion $(\mathbf{U}, \boldsymbol{\omega})$ such that

$$\mathbf{U} = \frac{\sigma}{\mu} S_{ijk}(\delta)[\mathbf{E}.\mathbf{e}_j][\mathbf{B}.\mathbf{e}_k]\mathbf{e}_i, \quad \boldsymbol{\omega} = \mathbf{0} \tag{25}$$

where the third-rank 'mobility' tensor $\mathbf{S} = S_{ijk}(\delta)\mathbf{e}_i \otimes \mathbf{e}_j \otimes \mathbf{e}_k$, solely depends upon the orthotropic particle geometry and relative conductivity δ and admits Cartesian components $S_{ijk}(\delta)$ that vanish with ε_{ijk}. Note that $\mathbf{U}$ vanishes when $\mathbf{E}$ and $\mathbf{B}$ are aligned but, in general, the orthotropic particle not necessarily translates parallel or antiparallel to $\mathbf{E} \wedge \mathbf{B}$ when $\mathbf{E} \wedge \mathbf{B} \neq \mathbf{0}$ although it becomes the case whenever $\mathbf{E}$ and $\mathbf{B}$ are normal to two different planes of symmetry. This section analytically obtains the six non-zero Cartesian components of the mobility tensor of a conducting ellipsoid and discusses in detail the predicted translation of either oblate or prolate conducting spheroids.

3.1 The analytical solution

Henceforth we consider the ellipsoid of relative conductivity $\delta \geq 0$ such that

$$x_1^2/a_1^2 + x_2^2/a_2^2 + x_3^2/a_3^2 = 1 \text{ for } \mathbf{x} = x_i\mathbf{e}_i \text{ on } S. \tag{26}$$

In this case (Jeffery (1922)) the surface forces $\mathbf{f}_T^{(i)}$ and $\mathbf{f}_R^{(i)}$ adopt, up to a constant multiple of the unit normal $\mathbf{n}$, the following forms (without summation over suffixes i in (27))

$$\begin{aligned} \mathbf{f}_T^{(i)} &= -\frac{4\mu s(\mathbf{x})}{[\chi + a_i^2\alpha_i]}, \\ \mathbf{f}_R^{(i)} &= -\frac{4\mu s(\mathbf{x})(\mathbf{e}_i \wedge \mathbf{x})}{[\chi - a_i^2\alpha_i]}, \end{aligned} \tag{27}$$

$$s(\mathbf{x}) = \left\{ \frac{x_1^2}{a_1^4} + \frac{x_2^2}{a_2^4} + \frac{x_3^2}{a_3^4} \right\}^{-1/2} \tag{28}$$

where the functions χ and α_i are defined as

$$\begin{aligned} \frac{\chi}{a_1a_2a_3} &= \int_0^\infty \frac{dt}{\gamma(t)}, \\ \frac{\alpha_i}{a_1a_2a_3} &= \int_0^\infty \frac{\gamma(t)^{-1}dt}{(a_i^2 + t)}, \end{aligned} \tag{29}$$

$$\gamma(t) = \sqrt{(a_1^2+t)(a_2^2+t)(a_3^2+t)}. \tag{30}$$

These results, of interest for numerical benchmarks in §4, clearly show that our coupling tensors $\mathbf{V}$ and $\mathbf{W}$, defined by (11)-(12), vanish. Accordingly, the vector $\mathbf{K}.\mathbf{U}$ is given by the right-hand side of (13). By superposition let us choose $\mathbf{B} = B\mathbf{e}_1$ and $\mathbf{E} = E\mathbf{e}_2$. For this electric field the material available in Lamb (1932) (see §111 – 114) yields, as detailed in Appendix B,

$$\begin{aligned} \nabla\phi' &= \frac{\alpha_2 d_2(\delta)E}{\alpha_2 - 2}\mathbf{e}_2 \text{ in } \mathscr{P}, \\ q &= \frac{2d_2(\delta)E}{\alpha_2 - 2}\mathbf{e}_2.\mathbf{n}, \end{aligned} \tag{31}$$

$$\nabla\phi.\mathbf{n} = d_2(\delta)E\mathbf{e}_2.\mathbf{n} \text{ on } S \tag{32}$$

where the unit normal $\mathbf{n}$ on S and the occurring coefficient $d_2(\delta)$ read

$$\mathbf{n}(\mathbf{x}) = \sum_{i=1}^{3} \frac{s(\mathbf{x})x_i}{a_i^2}\mathbf{e}_i, \;\; d_2(\delta) = \frac{(\delta-1)(\alpha_2-2)}{2 + (\delta-1)\alpha_2}. \tag{33}$$

At this stage, one may easily prove that $0 < \alpha_2 < 2$ and this legitimates the introduction of $d_2(\delta)$ in the entire range $\delta \geq 0$. If one denotes by ϕ_0 the perturbation potential outside the *same insulating* ellipsoid for the ambient electric field $\mathbf{E} = \mathbf{e}_2$, it follows from (29) and $d_2(0) = 1$ that $\phi = d_2(\delta)E\phi_0$ in the whole fluid domain Ω. Since

$\nabla\phi'$ is uniform in the solid $\mathscr{P}$ the equation (13) then becomes, after a few elementary algebra,

$$\mathbf{K}.\mathbf{U} = \frac{\sigma}{\mu} EBd_2(\delta)\left\{ \mathscr{V}_{\mathscr{P}}\mathbf{e}_1\wedge\mathbf{e}_2 - \left(\int_\Omega \mathbf{u}_T^{(i)}.[\nabla\phi_0\wedge\mathbf{e}_1]dv\right)\mathbf{e}_i\right\}. \quad (34)$$

Comparing (34) with (25) under the identity $d_2(0)=1$ yields the simple relation $S_{i21}(\delta) = d_2(\delta)S_{i21}(0)$ which permits us to deduce the required coefficient $S_{i21}(\delta)$ for the conducting ellipsoid from the coefficient $S_{i21}(0)$ obtained in Sellier (2003a) for the same *insulating* ellipsoid. Appealing to cyclic interchanges of suffixes and Sellier (2003a), we thus arrive at the desired analytical solution (without summation over suffixes i and j in (35))

$$S_{ijk}(\delta) = \frac{\varepsilon_{ijk}(\delta-1)(\alpha_i a_i^2+\alpha_j a_j^2)}{6[2+(\delta-1)\alpha_j]}. \quad (35)$$

By virtue of (35) and because $2+(\delta-1)\alpha_j>0$, two identical ellipsoids of different relative conductivities δ_1 and δ_2 clearly adopt for any setting $(\mathbf{E},\mathbf{B})$ a parallel or anti-parallel translation when $(\delta_1-1)(\delta_2-1)$ is positive or negative, respectively. For a sphere of radius a one obtains $\alpha_i = 2/3$ and (25), in conjunction with (35), takes the simple form

$$\mathbf{U} = c(\delta)\frac{\sigma a^2}{\mu}[\mathbf{E}\wedge\mathbf{B}] \text{ with } c(\delta) = \frac{\delta-1}{3(\delta+2)}; \quad (36)$$

a result in perfect agreement with Leenov and Kolin (1954) or Marty and Alemany (1984) (1984). The coefficient $c(\delta)$, plotted in Fig. 2(a) versus the sphere conductivity ratio δ, is negative or positive for $\sigma_s<\sigma$ or $\sigma_s>\sigma$ respectively and asymptotes to $1/3$ as the sphere becomes much more conducting than the surrounding fluid. Note that $c' = -6c$ compares the velocity of the conducting sphere to the velocity of the same *insulating* sphere. Since $c(4) = -c(0) = 1/6$, a conducting sphere moves faster or slower than if insulating when $\delta>4$ or $0<\delta<4$ respectively. For a non-spherical ellipsoid the velocity $\mathbf{U}$ is not in general aligned with $\mathbf{E}\wedge\mathbf{B}$. If we further denote by $\mathbf{U}(\delta',\Lambda)$ the velocity of a similar ellipsoid, of semi-axis $a_i' = \Lambda a_i$ with $\Lambda>0$ and relative conductivity $\delta' = \sigma_s'/\sigma \geq 0$, observe that, since $\alpha_i' = \alpha_i$, for any ambient magnetic field $\mathbf{B}$

$$\mathbf{U}(\delta,\Lambda) = \Lambda^2\mathbf{U}(\delta,1) \quad \text{for any electric field } \mathbf{E}, \quad (37)$$

$$\frac{(\delta-1)\mathbf{U}(\delta',\Lambda)}{[2+(\delta-1)\alpha_i]} = \frac{\Lambda^2(\delta'-1)\mathbf{U}(\delta,1)}{[2+(\delta'-1)\alpha_i]} \quad \text{if } \mathbf{E}\wedge\mathbf{e}_i = \mathbf{0}. \quad (38)$$

For instance, from (37) the velocity of a conducting ellipsoid is quarter of the velocity of the two times bigger and similar ellipsoid of identical conductivity for any setting $(\mathbf{E},\mathbf{B})$. For $\delta\neq 1$ one may also select $\delta'\neq\delta$ and Λ to obtain 'equivalent' ellipsoids, i.e. such that $\mathbf{U}(\delta',\Lambda) = \mathbf{U}(\delta,1)$. By virtue of (38), for $\mathbf{E}$ aligned with $\mathbf{e}_i$ an infinite number of solutions (δ',Λ) are found with

$$\delta' = \frac{(\delta-1)(2-\alpha_i)+\Lambda^2[2+(\delta-1)\alpha_i]}{\Lambda^2[2+(\delta-1)\alpha_i]+(1-\delta)\alpha_i}, \ \Lambda>\Lambda_c \quad (39)$$

and two different circumstances arise for the occurring critical value $\Lambda_c(\delta)$:

$$\Lambda_c(\delta) = \left\{\frac{(\delta-1)(\alpha_i-2)}{2+(\delta-1)\alpha_i}\right\}^{1/2} \leq 1, \quad \delta'<1 \text{ if } \delta<1, \quad (40)$$

$$\Lambda_c(\delta) = \left[\frac{(\delta-1)\alpha_i}{2+(\delta-1)\alpha_i}\right]^{1/2} < 1, \quad \delta'>1 \text{ if } \delta>1. \quad (41)$$

In addition to the trivial solution $(\delta',\Lambda) = (\delta,1)$ one thus always obtains a great deal of 'equivalent' ellipsoids. Note that δ' asymptotes to the unity when Λ becomes large but to be fully consistent with our low-Reynolds-number assumption one should have $\mathrm{Re}(\Lambda) = \Lambda\rho Ua/\mu \ll 1$ and this condition puts an upper bound to the above values of Λ. Furthermore, $\delta'\to\infty$ as $\Lambda\to\Lambda_c(\delta)$ for

$\delta > 1$ and (use (31)-(33)) the total electric field $\mathbf{E} - \nabla\phi'$ vanishes inside the similar ellipsoid of relative conductivity δ'.

Note that results (39)-(41) hold for $\mathbf{E}$ aligned with $\mathbf{e}_i$ and two ellipsoids 'equivalent' for $\mathbf{E} \wedge \mathbf{e}_i = \mathbf{0}$ are, in general, not 'equivalent' any more when $\mathbf{E} \wedge \mathbf{e}_j = \mathbf{0}$ and $j \neq i$. Notable exceptions are spherical and spheroidal particles which exhibit additional symmetries. For example (see (36) or set $\alpha_i = 2/3$ in (39)-(41)), the sphere of radius Λa and relative conductivity δ' experiences the same non-zero translation as the sphere of radius a and given relative conductivity $\delta \neq 1$, whatever the ambient electric and magnetic fields $\mathbf{E}$ and $\mathbf{B}$, only if it is large enough, i. e. for $\Lambda > \Lambda_c(\delta)$, and it admits the relative conductivity δ' such that

$$\delta' = \frac{2(\delta-1)+\Lambda^2(\delta+2)}{\Lambda^2(\delta+2)+(1-\delta)}, \tag{42}$$

$$\Lambda_c(\delta) = \left[\frac{3|\delta-1|+1-\delta}{2(\delta+2)}\right]^{1/2} \text{ with } \delta \neq 1. \tag{43}$$

The above function δ' is plotted versus the size parameter Λ for a few values of the relative conductivity δ of the sphere of radius a in Fig. 2(b). Clearly, the relative conductivity δ' of 'equivalent' spheres of radius roughly smaller than $3a$ is seen to deeply depend upon the conductivity ratio δ of the sphere of radius a. By contrast, $\delta' \sim 1$ for 'equivalent' bigger spheres ($\Lambda \gtrsim 3$) whatever the value of δ.

The analysis also shows that two similar spheroids of axis of revolution parallel to $\mathbf{e}_3$ are 'equivalent', i. e. translate at the same velocity, for any setting $(\mathbf{E}, \mathbf{B})$ such that $\mathbf{E}.\mathbf{e}_3 = 0$ as soon as δ' and Λ satisfy (39)-(41) for $i = 1$ (or $i = 2$). As discussed in the next subsection, non-similar spheroids of axis of revolution parallel to $\mathbf{e}_3$ may also become 'equivalent' if $\mathbf{E}.\mathbf{e}_3 = 0$ for other values of δ'.

3.2 Application to spheroidal particles

Let us denote by $\mathscr{S}(a,\lambda)$ the spheroid of axis of revolution aligned with $\mathbf{e}_3$ such that $a_1 = a_2 = a$ and $a_3 = \lambda a$. This spheroid is oblate or prolate for $\lambda < 1$ or $\lambda > 1$ respectively and one easily obtains $\alpha_1 = \alpha_2 = \alpha(\lambda)$ and $\alpha_3 = \beta(\lambda)$ with (Sellier (2003a)) the relations

$$\alpha(\lambda) = \frac{\lambda^2}{\lambda^2-1}\left[1 - \frac{g(\lambda)}{2\lambda^2\sqrt{\lambda^2-1}}\right], \tag{44}$$

$$\beta(\lambda) = \frac{1}{\lambda^2-1}\left[\frac{\lambda g(\lambda)}{\sqrt{\lambda^2-1}} - 2\right], \tag{45}$$

$$g(\lambda) = \log\left[2\lambda^2 + 2\lambda\sqrt{\lambda^2-1} - 1\right] \text{ if } \lambda > 1, \tag{46}$$

$$g(\lambda) = 2\arctan\left[\frac{\sqrt{1-\lambda^2}}{\lambda}\right] \text{ if } \lambda < 1. \tag{47}$$

In addition, (35) immediately yields $S_{123} = -S_{213} = a^2 c_1(\delta,\lambda), S_{231} = -S_{132} = a^2 c_2(\delta,\lambda)$ and $S_{312} = -S_{321} = a^2 c_3(\delta,\lambda)$ where the occurring coefficients are defined as

$$c_1 = \frac{(\delta-1)\alpha}{3[2+(\delta-1)\alpha]}, \qquad c_2 = \frac{(\delta-1)(\alpha+\lambda^2\beta)}{6[2+(\delta-1)\beta]}, \tag{48}$$

$$c_3 = \frac{(\delta-1)(\alpha+\lambda^2\beta)}{6[2+(\delta-1)\alpha]}. \tag{49}$$

Note that as δ becomes large then $c_1 \sim 1/3$ for any shape parameter λ, i. e. any spheroid $\mathscr{S}(a,\lambda)$ of large conductivity behaves like a sphere of radius a in Case 1. By contrast, c_2 and c_3 tend to finite limit that are shape-dependent as δ increases. As already pointed out for insulating spheroidal particles ($\delta = 0$) in Sellier (2003a) and readily still valid for any conducting spheroid, the velocity $\mathbf{U}$ is aligned with $\mathbf{E} \wedge \mathbf{B}$ and depends solely upon one of the previous coefficients c_k for the following special settings

$$\text{Case 1: } \mathbf{B}||\mathbf{e}_3 \text{ or } \mathbf{E}.\mathbf{e}_3 = (\mathbf{E}\wedge\mathbf{B}).\mathbf{e}_3 = 0, \tag{50}$$

$$\text{Case 2: } \mathbf{E}||\mathbf{e}_3 \text{ or } \mathbf{B}.\mathbf{e}_3 = (\mathbf{E}\wedge\mathbf{B}).\mathbf{e}_3 = 0, \tag{51}$$

$$\text{Case 3: } \mathbf{e}_3||\mathbf{E}\wedge\mathbf{B}, \tag{52}$$

which are sketched in Fig. 3(a)-3(c).

In such circumstances, the translational velocity $\mathbf{U}$ indeed reads

$$\mathbf{U} = c_k(\delta,\lambda)\frac{\sigma a^2}{\mu}[\mathbf{E}\wedge\mathbf{B}] \text{ in Case } k = 1,2,3. \tag{53}$$

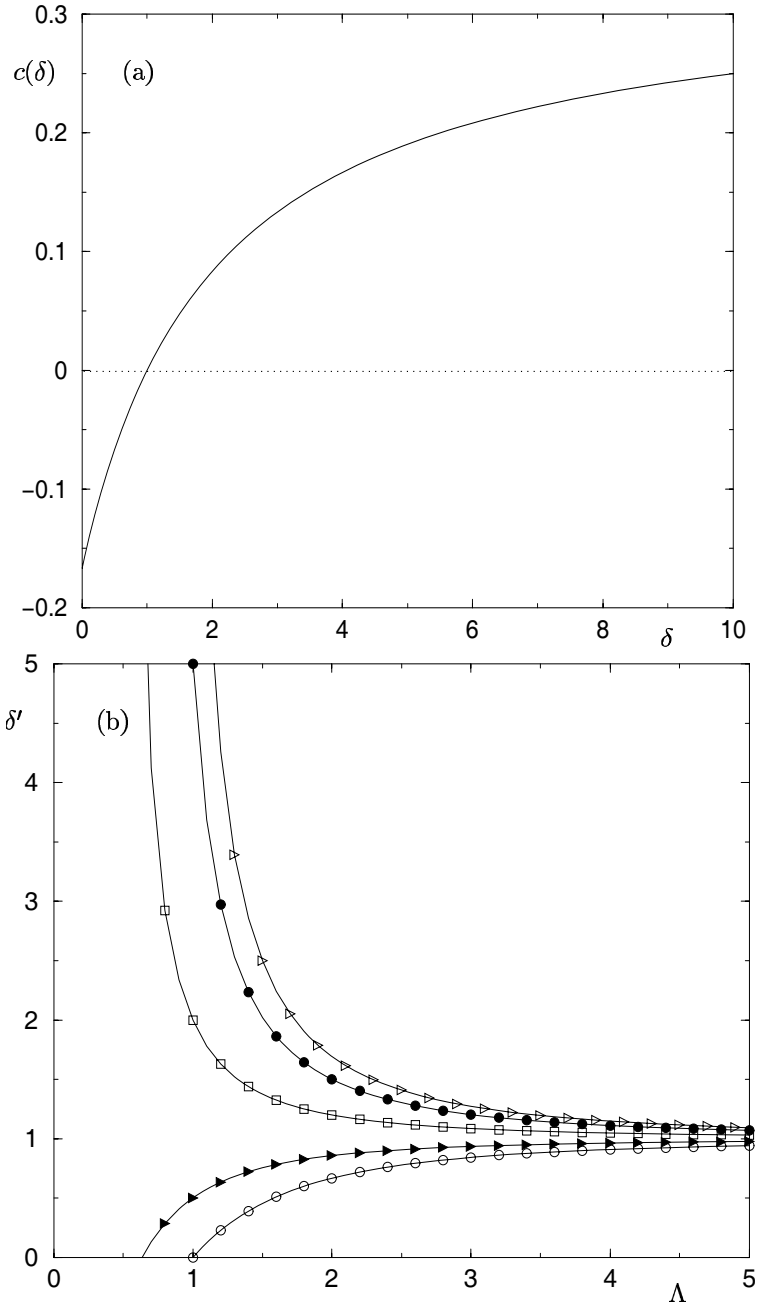

Figure 2: (a) Coefficient $c(\delta)$, as defined in equation (36), for spheres of relative conductivity δ. (b) Location in the $\Lambda - \delta'$ plane of the 'equivalent' spheres of radius Λa and relative conductivity δ' that experience the same translation as the sphere of radius a and conductivity ratio $\delta' \neq 1$, for $\delta = 0$ ($\circ$), $\delta = 0.5$ ($\blacktriangleright$), $\delta = 2$ ($\square$), $\delta = 5$ ($\bullet$) and $\delta = 10$ ($\triangleright$).

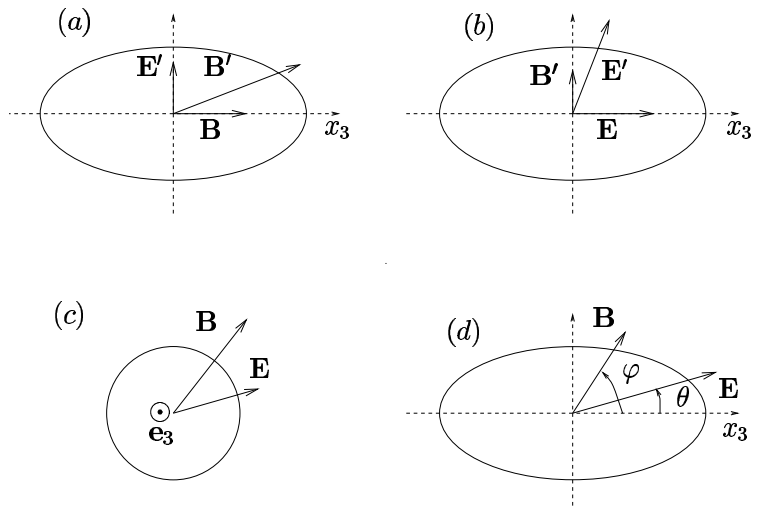

Figure 3: Illustration of Cases 1,2,3 and 4 for which **U** is aligned with $\mathbf{E}\wedge\mathbf{B}$. (a) Possible settings $\mathbf{B}||\mathbf{e}_3$ or $(\mathbf{E}',\mathbf{B}')$ in Case 1. (b) Possible settings $\mathbf{E}||\mathbf{e}_3$ or $(\mathbf{E}',\mathbf{B}')$ in Case 2. (c) Possible setting $(\mathbf{E},\mathbf{B})$ in Case 3. (d) Employed notations and ambient electric and magnetic fields **E** and **B** in Case 4.

For convenience, let us denote by $S_{ve}(\delta)$ the sphere of relative conductivity δ that has the same volume as the spheroid $\mathscr{S}(a,\lambda)$, i. e. of radius $\lambda^{1/3}a$. Instead of plotting the coefficients c_k we rather show in Fig. 4(a)-4(b) each function $c'_k=-6c_k\lambda^{-2/3}$ which compares the spheroid velocity in Case k to the velocity of the volume equivalent and *insulating* sphere $S_{ve}(0)$.

The spheroid translates parallel or anti-parallel to $S_{ve}(0)$ for $\delta<1$ or $\delta>1$ respectively and faster above and below horizontal long-dashed lines. For comparisons the case of the volume equivalent sphere of the same relative conductivity $S_{ve}(\delta)$, in other words the previously alluded to function $c'=-6c$, is plotted as a solid curve in Fig. 4(a)-(b). Clearly, the behavior of both oblate and prolate spheroids deeply depends upon the selected Case k and the sign of $\delta-1$. As depicted in Fig. 4(a), oblate spheroids translate faster, and more faster as $\lambda\geq 1/5$ decreases, than the volume equivalent conducting sphere $S_{ve}(\delta)$ in Case 2 for $\delta<1$ and in Case 1 for $\delta>1$. In Case 3 opposite or similar trends are found when δ is of medium value $1\leq\delta\lesssim 5$ or not, respectively. As evidenced in Fig. 4(b), prolate spheroids exhibit another sensitivity to Cases k. This time, the prolate spheroid moves slower than its volume equivalent sphere $S_{ve}(\delta)$ except in Case 2 for $\delta>1$ and in Case 3 for $\delta<1$. In any case, the difference in velocity with $S_{ve}(\delta)$ increases with the slenderness ratio λ. Finally, one should note that for $\delta<1$ curves c_1 and c_2 cross for $\lambda=1/5,1/2,2$. The ratio c_1/c_2, which compares the spheroid velocity in Cases 1 and 2 (for the same magnitude of different settings $\mathbf{E}\wedge\mathbf{B}$), is incidentally the slope at origin of the curves shown in Fig. 6(b) for $\delta=0,2$ and the same values of the shape parameter λ. These slopes illustrate the strong sensitivity of the incurred translation to the selected Cases 1 and 2 for $\lambda=1/5,1/2,2$.

Finally, the sensitivity of the coefficients c'_k to the shape parameter λ is shown in Fig. 5(a)-5(b) for $\delta=0$ and $\delta=2$. These figures clearly illustrate the significant dependence of the spheroid velocity to the selected Case k and its nature (oblate or prolate). Contrary to the case of an insulating spheroid (which has been discussed in detail in Sellier (2003a)) the spheroid of relative conductivity $\delta=2$ is seen to move slower than its equivalent insulating sphere $\mathscr{S}_{ve}$ in any circumstance. In addition, a given spheroid (λ prescribed and $\delta=2$) experiences its greatest and smallest velocity in Cases 1 and 2 respectively if oblate ($\lambda<1$) and Cases 2 and 1 respectively if prolate ($\lambda>1$).

In previous Cases k the velocity **U** is aligned with $\mathbf{E}\wedge\mathbf{B}\neq\mathbf{0}$ and only vanishes for $\delta=1$. By a

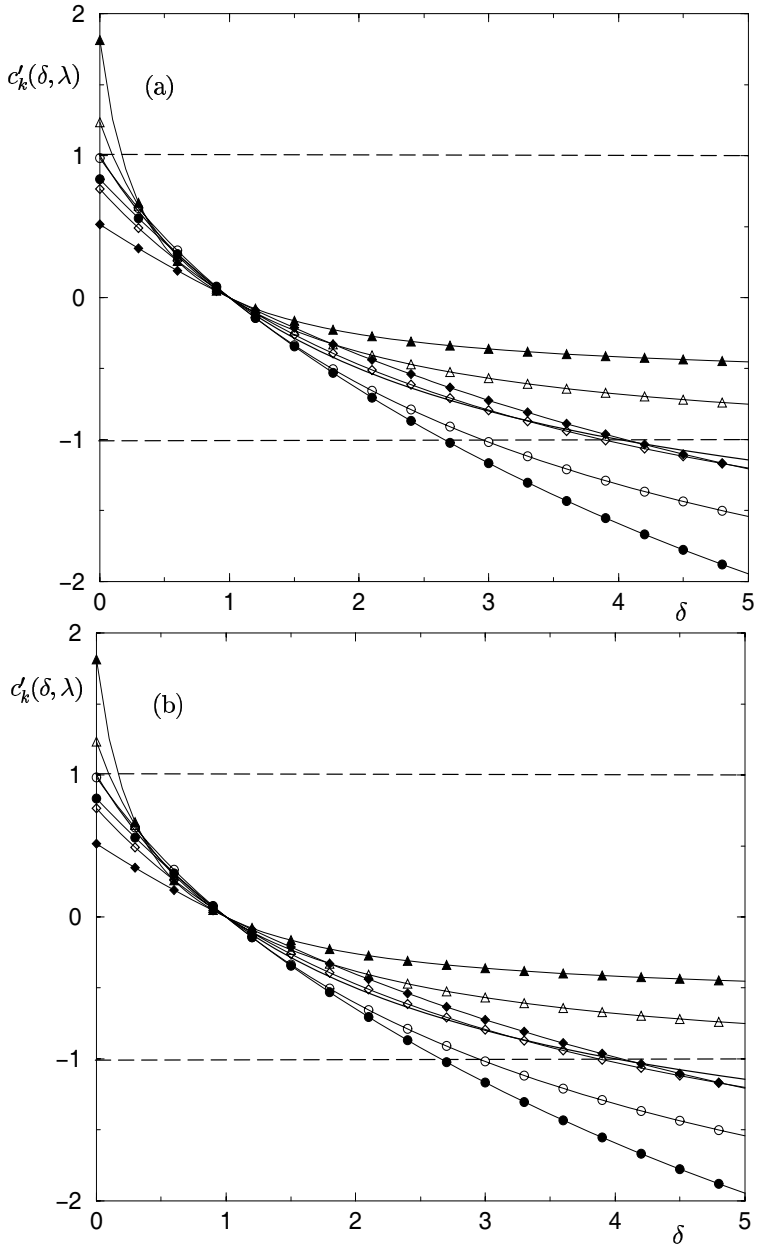

Figure 4: Normalized functions c'_k for spheroids with the case of a conducting sphere recalled by the solid curve. (a) Oblate spheroids in Case 1 ($\circ$ for $\lambda = 1/2$ and $\bullet$ for $\lambda = 1/5$), Case 2 ($\triangle$ for $\lambda = 1/2$ and $\blacktriangle$ for $\lambda = 1/5$) and Case 3 ($\Diamond$ for $\lambda = 1/2$ and $\blacklozenge$ for $\lambda = 1/5$). (b) Prolate spheroids in Case 1 ($\circ$ for $\lambda = 1/2$ and $\bullet$ for $\lambda = 1/5$), Case 2 ($\triangle$ for $\lambda = 1/2$ and $\blacktriangle$ for $\lambda = 1/5$) and Case 3 ($\Diamond$ for $\lambda = 1/2$ and $\blacklozenge$ for $\lambda = 1/5$).

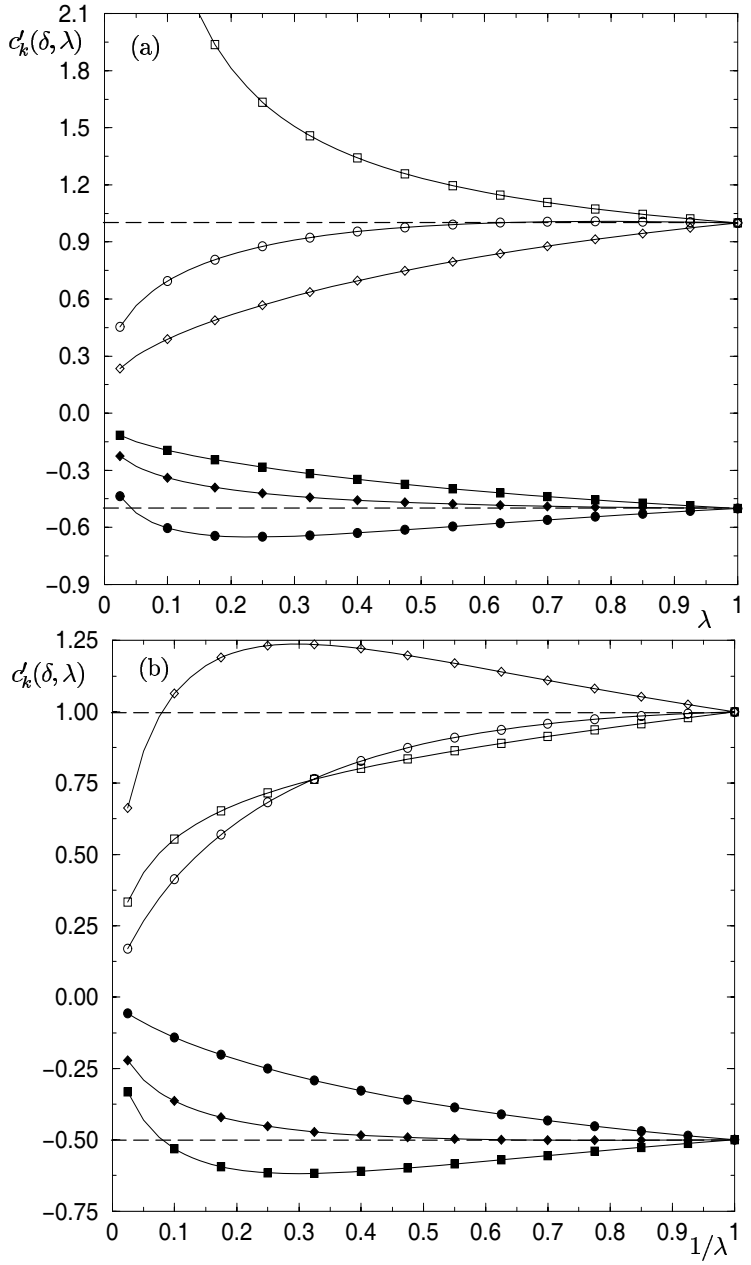

Figure 5: Normalized functions c'_k in Cases k for $\delta = 0$ ($\circ$ for $k = 1, \square$ for $k = 2, \Diamond$ for $k = 3$) and $\delta = 2$ ($\bullet$ for $k = 1, \blacksquare$ for $k = 2, \blacklozenge$ for $k = 3$). The horizontal long-dashed lines indicate the values for a spherical particle ($\lambda = 1$). (a) Case of oblate spheroids: $\lambda < 1$. (b) Case of problate spheroids: $\lambda > 1$.

straightforward extension of the available results for insulating spheroids, i. e. by replacing in Sellier (2003a) each encountered term $-C_k$ with the previous coefficient c_k, it is found that $\mathbf{U}$ is also aligned with the non-zero product $\mathbf{E}\wedge\mathbf{B}$ only in the following additional Case 4:

$$\mathbf{E}\wedge\mathbf{B}\neq\mathbf{0},\quad (\mathbf{E}\wedge\mathbf{B}).\mathbf{e}_3=0,\quad (\mathbf{E}.\mathbf{e}_3)(\mathbf{B}.\mathbf{e}_3)\neq 0. \tag{54}$$

In such circumstances $\mathbf{E},\mathbf{B}$ and $\mathbf{e}_3$ lie in the same plane and the translation $\mathbf{U}$ is normal to $\mathbf{e}_3$ but does not depend solely upon one coefficient c_k. Furthermore, it is possible to select $(\mathbf{E},\mathbf{B})$ so that $\mathbf{U}$ vanish although $\mathbf{E}\wedge\mathbf{B}$ and $\delta-1$ are non-zero. For example, if we take $0<\theta=(\mathbf{E},\mathbf{e}_3)<\pi/2$ and $0<\varphi=(\mathbf{B},\mathbf{e}_3)\leq\pi/2$, as illustrated in Fig. 3(d), the translation $\mathbf{U}$ vanishes when $\delta\neq 1$ for (exploit Sellier (2003a))

$$\begin{aligned}\tan\varphi&=\frac{c_1(\delta,\lambda)}{c_2(\delta,\lambda)}\\ \tan\theta&=\frac{2\alpha[2+(\delta-1)\beta]\tan\theta}{(\alpha+\lambda^2\beta)[2+(\delta-1)\alpha]}.\end{aligned} \tag{55}$$

Of course, solutions of interest $\varphi\neq\theta$ and sensitive to the spheroid relative conductivity δ and the shape parameter λ. As shown in Fig. 6(a), the critical angle φ associated to the case $\theta=\pi/4$ strongly depends upon these parameters. The solution (φ,θ), dictated by (55), is plotted in Fig. 6(b) for $\delta=0,2$ and $\lambda=1/5,1/2,2,5$. Since (55) readily becomes $\varphi=c_1\theta/c_2$ as θ vanishes, the slope of each curve at the origin indeed provides, as previously announced, the ratio $c_1/c_2=c_1'/c_2'$ for the selected pair (δ,λ). Note that $\varphi-\theta$ is weak for nearly insulating spheroids (δ small) except for thin oblate spheroids ($\lambda\ll 1$). For $\delta=2$ (and above this value) the critical angle φ deeply depends upon the spheroid shape parameter λ and becomes significantly greater or smaller than θ for oblate or prolate spheroids, respectively.

Let us now look at similar spheroids $\mathscr{S}(\Lambda a,\lambda)$ of relative conductivity δ' that are 'equivalent' to the spheroid $\mathscr{S}(a,\lambda)$ of conductivity ratio δ for a specified setting $(\mathbf{E},\mathbf{B})$. For symmetry reasons, our results (39)-(41) for $i=1$ or $i=3$ provide the answer for $\mathbf{E}.\mathbf{e}_3=0$ or $\mathbf{E}\wedge\mathbf{e}_3=\mathbf{0}$ respectively, whatever the ambient magnetic field $\mathbf{B}$. The curves, associated to a prescribed value of δ, are located in the $\Lambda-\delta'$ plane in Fig. 7(a)-7(b) for $\lambda=1/5$ and $\lambda=5$. Clearly, the solution (Λ,δ') is nearly the one obtained for a sphere for prolate spheroids of vanishing relative conductivity δ if $\mathbf{E}.\mathbf{e}_3=0$ and spheroidal particles of conductivity ratio $\delta=O(1)$ with $\Lambda\gtrsim 1$ for any ambient electric field $\mathbf{E}$. By contrast, (Λ,δ') is found to deeply depend upon the shape parameter λ for oblate spheroids of vanishing conductivity if $\mathbf{E}\wedge\mathbf{e}_3=\mathbf{0}$ and both oblate or prolate spheroids of large relative conductivity ($\delta\gtrsim 10$) for any electric field $\mathbf{E}$.

Finally, one should note that two non-similar spheroids $\mathscr{S}(a,\lambda_1)$ and $\mathscr{S}(a,\lambda_2)$ of relative conductivities $\delta_1\neq\delta_2$ may experience the same translation for a given setting $(\mathbf{E},\mathbf{B})$. For example, in Fig. 4(a) oblate spheroids of shape parameters $\lambda_2=1/5$ and $\lambda_1=1/2$ are 'equivalent' in Case 2 (to the same insulating sphere $\mathscr{S}(a,1)$) for critical values $\delta_2\sim 0.17$ and $\delta_1\sim 0.10$ and 'equivalent' in Case 1 (with this time the opposite velocity of the insulating sphere $\mathscr{S}(a,1)$) for the critical values $\delta_2\sim 2.65$ and $\delta_1\sim 2.94$.

Before closing this subsection it is worth pointing out that for any orthotropic and axisymmetric particle, of axis of symmetry parallel to $\mathbf{e}_3$ and typical length scale a, we again have $S_{123}=-S_{213}=a^2c_1, S_{231}=-S_{132}=a^2c_2$ and $S_{312}=-S_{321}=a^2c_3$ with coefficients c_1,c_2 and c_3 determined solely by the particle geometry and relative conductivity δ. Of course, the property (53) in Cases 1-3 and the key relation $\tan\varphi=c_1\tan\theta/c_2$ for the critical orientations (θ,φ) in Case 4 still hold. For instance, these remarks hold for any conducting torus of axis of symmetry parallel to $\mathbf{e}_3$; a geometry which is numerically addressed in the next section.

4 Relevant boundary-integral equations and numerical method

This section presents boundary-integral equations that make it possible to compute, in practice for an arbitrarily-shaped conducting particle of smooth enough boundary, the required surface forces $\mathbf{f}_T^{(i)},\mathbf{f}_R^{(i)}$, the polarization surface-charge density q and not only the perturbation potential ϕ but also

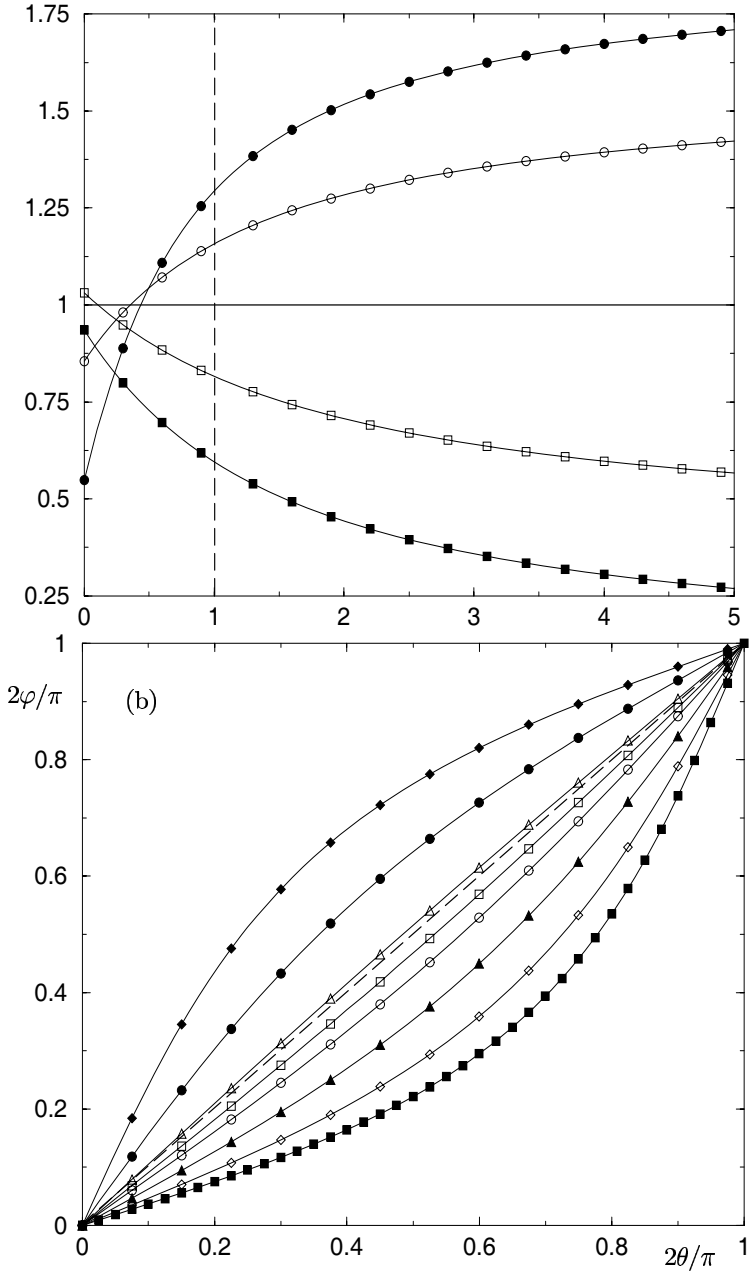

Figure 6: (a) Function $4\varphi/\pi$ with φ the critical angle (defined by (3.24)) if $\theta = \pi/4$ for $\lambda = 1/5$ ($\bullet$), $\lambda = 1/2$($\circ$), $\lambda = 2$ ($\square$) and $\lambda = 5$ ($\blacksquare$). (b) Critical settings (θ, φ) for spheroidal particles of relative conductivity $\delta = 0$ (clear symbols) or $\delta = 2$ (filled symbols) and shape parameter $\lambda = 1/5$ (diamonds), $\lambda = 1/2$ (circles), $\lambda = 2$ (triangles) and $\lambda = 5$ (squares). On the long-dashed line **B** is aligned with **E**, i. e. $\varphi = \theta$.

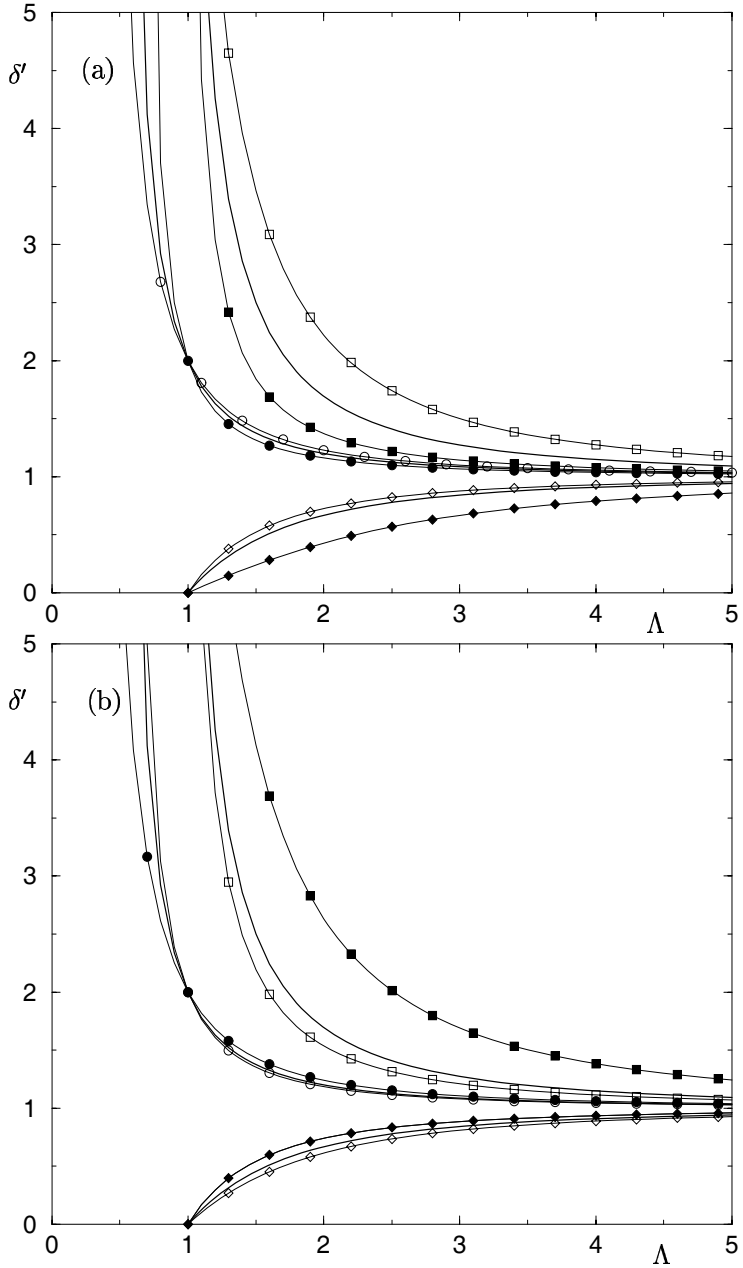

Figure 7: Location in the $\Lambda - \delta'$ plane of spheroidal particles $\mathscr{S}(\Lambda a, \lambda)$ of relative conductivity δ' that adopt, for any magnetic electric field $\mathbf{B}$, the translation of the spheroid $\mathscr{S}(a, \lambda)$ of conductivity ratio δ if $\mathbf{E}.\mathbf{e}_3 = 0$ (clear symbols) or $\mathbf{E} \wedge \mathbf{e}_3 = \mathbf{0}$ (filled symbols). The case of spherical particles, depicted in Fig. 2(b), is recalled by solid curves. (a) Case of oblate spheroids of shape parameter $\lambda = 1/5$ for $\delta = 0$ (clear or filled diamonds), $\delta = 2$ (clear or filled circles) and $\delta = 10$ (clear or filled squares). (b) Case of prolate spheroids of shape parameter $\lambda = 5$ for $\delta = 0$ (clear or filled diamonds), $\delta = 2$ (clear or filled circles) and $\delta = 10$ (clear or filled squares).

the gradient $\nabla\phi = \phi_{,m}\mathbf{e}_m$ and the normal fluxes $\nabla(\phi_{,m}).\mathbf{n}$ on the particle surface S. As emphasized in §2, the rigid-body motion $(\mathbf{U},\boldsymbol{\omega})$ is then immediately deduced from these quantities by exploiting (11)-(15) and (19)-(22).

4.1 Advocated boundary-integral equations

Let us start with the determination of vectors $\mathbf{f}_T^{(i)}$ and $\mathbf{f}_R^{(i)}$. For $L \in \{T,R\}$, recall that $\mathbf{f}_L^{(i)}$ is the surface force induced on the particle boundary by the steady Stokes flow $\mathbf{u}_L^{(i)}$, free from body forces, quiescent at infinity and such that $\mathbf{u}_T^{(i)} = \mathbf{e}_i$ or $\mathbf{u}_R^{(i)} = \mathbf{e}_i \wedge \mathbf{x}$ on S. Due to the very specific nature of those rigid-body boundary conditions, such a Stokes flow admits in the whole fluid domain Ω a single-layer representation (Pozrikidis (1992)) that reads on the surface S

$$\int_S \left[\mathbf{f}_L^{(i)}.\mathbf{e}_k\right](P)\left[\frac{\delta_{jk}}{PM} + \frac{(\mathbf{PM}.\mathbf{e}_j)(\mathbf{PM}.\mathbf{e}_k)}{PM^3}\right] dS_P = -8\pi\mu\left[\mathbf{u}_L^{(i)}.\mathbf{e}_j\right](M) \quad \text{for } M \text{ on } S \tag{56}$$

where δ_{jk} denotes the usual Kronecker Delta. The above key Fredholm boundary-integral equation of the first kind is known (Ladyzhenskaya (1969)) to admit a solution $\mathbf{f}_L^{(i)}$ unique up to an arbitrary multiple of the unit normal $\mathbf{n}$. As previously pointed out, each second-rank tensor $\mathbf{K},\mathbf{V},\mathbf{W}$ or $\mathbf{D}$ and the right-hand sides of equations (13)-(14) are however uniquely determined.

Using the single-layer representation (16), both for ϕ' and ϕ, it is also straightforward to cast the identity (18) into the following form

$$[\delta+1]\frac{q(M)}{2} + [1-\delta]\int_S \frac{\mathbf{PM}.\mathbf{n}(M)}{4\pi PM^3} q(P) dS_P = [\delta-1][\mathbf{E}.\mathbf{n}](M) \quad \text{for } M \text{ on } S. \tag{57}$$

Because $\delta \geq 0$, the Fredholm boundary-integral equation of the second kind (57) is well-posed (see Zabreyko (1975), p.215). Upon using for M on the surface S the following identity and definition

$$\int_S \frac{\mathbf{MP}.\mathbf{n}(P)}{4\pi PM^3} dS_P = \frac{1}{2} \tag{58}$$

$$J_\delta(M) = \delta + (1-\delta)\int_S \frac{\mathbf{PM}.[\mathbf{n}(M)-\mathbf{n}(P)]}{4\pi PM^3} dS_P \tag{59}$$

it is useful for its numerical treatment to rewrite (57) as

$$[1-\delta]\int_S \frac{[q(P)-q(M)]\mathbf{PM}.\mathbf{n}(M)}{4\pi PM^3} dS_P + [J_\delta q](M) = [\delta-1][\mathbf{E}.\mathbf{n}](M). \tag{60}$$

The above equivalent formulation, which only involves weakly-singular integrals, is indeed quite suitable for our numerical implementation.

Finally, we need to evaluate, on the particle surface S *only*, the perturbation potential ϕ subject to the well-posed exterior Neumann problem (23)-(24) together with its gradient $\nabla\phi = \phi_{,m}\mathbf{e}_m$ and the normal fluxes $\nabla(\phi_{,m}).\mathbf{n}$. Appealing to the decaying far-field behavior of ϕ and the usual second Green's identity, we easily arrive (Bonnet (1999)) at the boundary relation

$$-4\pi\phi(M) + \int_S [\phi(P)-\phi(M)]\frac{\mathbf{PM}.\mathbf{n}(P)}{PM^3} dS_P = \int_S \frac{[\mathbf{E}.\mathbf{n}](P)}{PM} dS_P \quad \text{for } M \text{ on } S. \tag{61}$$

From the knowledge of the normal flux $\nabla.\mathbf{n} = \mathbf{E}.\mathbf{n} - \delta q/(\delta-1)$ we thus obtain the required value of ϕ on the whole surface S by solving the Fredholm boundary-integral equation of the second kind (61). At this stage, one may approximate the gradient $\nabla\phi$ on the surface S by computing tangential derivatives of ϕ and using the prescribed normal derivative $\nabla\phi.\mathbf{n}$. However, another treatment is needed in accurately evaluating the required quantities $\nabla(\phi_{,m}).\mathbf{n}$. on S. The advocated strategy, both established and numerically tested in Sellier (2003b), makes use of one additional boundary-integral equation that relates on S the cartesian derivatives of any function ψ, harmonic in Ω and such that $r\psi \to 0$ as $r \to \infty$. More precisely, if we introduce on the boundary S the usual mean curvature C, the tangential derivatives $D_{ij}\psi$ (Duduchava (2001)) such that

$$C(M) = [\nabla.\mathbf{n}](M), \tag{62}$$

$$[D_{ij}\psi](M) = [\mathbf{n}.\mathbf{e}_i](M)\psi_{,j}(M) - [\mathbf{n}.\mathbf{e}_j](M)\psi_{,i}(M) \tag{63}$$

and the weakly-singular surface integrals $I_i(M)$ as

$$I_i(M) = 2\pi[\mathbf{n}.\mathbf{e}_i](M) + \int_S \left\{ \frac{\mathbf{MP}.[\mathbf{n}(P)-\mathbf{n}(M)]}{PM^2} - C(P) \right\} \frac{\mathbf{n}(P).\mathbf{e}_i}{PM} dS_P, \tag{64}$$

the following key boundary-integral equation holds (Sellier (2003b))

$$\begin{aligned} &2\pi\psi_{,i}(M) - [D_{ij}\psi](M) I_j(M) \\ &+ \int_S \left\{ \frac{[D_{ij}\psi](P)-[D_{ij}\psi](M)}{PM^3} \right\} \mathbf{PM}.\mathbf{e}_j dS_P \\ &= \int_S [\frac{[\nabla\psi.\mathbf{n}](P)-[\nabla\psi.\mathbf{n}](M)}{PM^3}] \mathbf{PM}.\mathbf{e}_i dS_P \\ &\qquad - [\nabla\psi.\mathbf{n}](M) I_i(M) \quad \text{for } M \text{ on } S. \end{aligned} \tag{65}$$

Clearly, from the normal flux $\nabla\psi.\mathbf{n}$ and the mean curvature C one thus obtains the first-order cartesian derivatives $\psi_{,i}$ by solving the Fredholm boundary-integral equation of the second kind (65). In summary, the advocated strategy to compute $\phi, \phi_{,m} = \nabla\phi.\mathbf{e}_m$ and $\nabla(\phi_{,m}).\mathbf{n}$ on S then consists of three steps:

1) Calculate ϕ on S by solving (61).

2) Obtain the first-order cartesian derivatives $\phi_{,m}$ on S by exploiting (65) for $\psi = \phi$.

3) Evaluate, successively for $m = 1,2,3$ and by noting that $\phi_{,m}$ is harmonic in Ω and exhibits a good far-field behavior, the normal flux $\nabla(\phi_{,m}).\mathbf{n}$ by solving (61) for $\phi_{,m}$.

As demonstrated in Sellier (2003b), such a procedure yields accurate approximations of $\phi, \phi_{,m}$ and $\nabla(\phi_{,m}).\mathbf{n}$ on the surface.

4.2 Numerical method

In the past decades the challenging numerical treatment of either weakly-singular and regular boundary-integral eauqtions has received a considerable attention and played a key role in quite different fields. In that direction one should mention, for instance, the recent works by Hsiao and Ingber (2004), Gardano and Dabnichki (2006), Duddeck (2006) and Sanz et al (2007). In the present work we resort to a collocation method similar to the one employed in Sellier and Pasol (2006). More precisely, each encountered boundary-integral equation (56), (60), (61) or (65) is discretized and numerically inverted by using isoparametric boundary elements. Since this method has become standard, we briefly describe the employed steps and direct for additional details the reader to the available textbooks (see, among others, Beskos (1987), Pozrikidis (1992), Brebbia et al (1984) and Bonnet (1999)).

We employ on S a $N-$node mesh of N_e six-node curvilinear (quadratic) and isoparametric boundary elements Δ_e which are mapped onto the standard triangle Δ of inequations $0 \le \xi_1 \le 1, 0 \le \xi_2 \le 1$ and $\xi_1 + \xi_2 \le 1$ in plane cartesian and intrinsic coordinates $\xi = (\xi_1, \xi_2)$ by the quadratic shape functions

$$\begin{aligned} &\lambda_1(\xi) = (1-2\xi_1-2\xi_2)(1-\xi_1-\xi_2), \\ &\frac{\lambda_4(\xi)}{4} = \xi_1\xi_2, \end{aligned} \tag{66}$$

$$\begin{aligned} &\lambda_2(\xi) = 4\xi_1(1-\xi_1-\xi_2), \\ &\lambda_3(\xi) = (2\xi_1-1)\xi_1, \end{aligned} \tag{67}$$

$$\begin{aligned} &\lambda_5(\xi) = (2\xi_2-1)\xi_2, \\ &\lambda_6(\xi) = 4\xi_2(1-\xi_1-\xi_2). \end{aligned} \tag{68}$$

On each isoparametric element Δ_e, of nodal points $\mathbf{y}^{(e,m)}$ with $m \in \{1,...,6\}$, any function v is then interpolated as follows

$$v(P) = \sum_{m=1}^{6} \lambda_m(\xi) v^{(e,m)}, \quad v^{(e,m)} = v\left(\mathbf{y}^{(e,m)}\right) \tag{69}$$

$$\mathbf{OP} = \mathbf{OP}(\xi) = \sum_{m=1}^{6} \lambda_m(\xi) \mathbf{y}_l^{(e,m)}. \tag{70}$$

The evaluation of each boundary-integral equation at the nodal point $\mathbf{x} = \mathbf{OM}$ then appeals to the general integrals

$$I(M) = \int_S v(P) K[M,P] dS_P = \sum_{e=1}^{N_e} \sum_{m=1}^{6} v^{(e,m)} I_M^{(e,m)}, \tag{71}$$

$$I_M^{(e,m)} = \int_{\Delta_e} \lambda_m(\xi) K[\mathbf{x}, \mathbf{y}(\xi)] J(\xi) d\xi, \tag{72}$$

where K is a kernel of $1/PM$ type weak singularity and J denotes the jacobian of the mapping $\mathbf{y} = \mathbf{y}(\xi)$. Each integral $I_M^{(e,m)}$ is approximated by using standard Gaussian quadratures (Lyness and Jespersen (1975)). The quadrature order (accuracy), which depends upon the location of M, is selected as in Rezayat et al (1986) and the weak singularity is removed by appealing to polar coordinates centered at M whenever this point lies on the boundary element Δ_e. Accordingly, any discretized boundary-integral equation of interest becomes a $N'-$equation linear system $AX = Y$ (with $N' = N$ for (57) or (61) and $N' = 3N$ for (56) or(65)) of dense and non-symmetric influence matrix A. Note that, on theoretical ground, (56) is ill-posed but in practice (**?**, Pozrikidis (1992)) the associated matrix A is nonsingular unless very fine meshes are used. Any encountered system $AX = Y$ is thus numerically solved by a standard LU factoriztion algorithm (subroutines DGETRF and DGETRS of the Lapack Library).

5 Numerical results and discussion

This section first tests the numerical treatment advocated in §4 against the analytical solution obtained in §3.2 for conducting spheroids and then both presents and discusses numericals results for a few conducting tori and pear-shaped particles.

5.1 Case of conducting spheroids

As introduced in §3.2, we consider a conducting spheroid of shape parameter $\lambda > 0$ such that $a_1 = a_2$ and $a_3 = \lambda a$. Recalling the definition (28) of $s(\mathbf{x})$, the unit normal $\mathbf{n}(\mathbf{x})$ and the mean curvature $C(M) = C(\mathbf{x})$ then read

$$\mathbf{n}(\mathbf{x}) = \frac{s(\mathbf{x})}{a^2}\left[x_1\mathbf{e}_1 + x_2\mathbf{e}_2 + \frac{x_3}{\lambda^2}\mathbf{e}_3\right], \tag{73}$$

$$C(\mathbf{x}) = \frac{s(\mathbf{x})}{a^2}\left[2 + \lambda^{-2} - \frac{s^2(\mathbf{x})}{a^4}\left(x_1^2 + x_2^2 + \frac{x_3^2}{\lambda^6}\right)\right]. \tag{74}$$

Any point M on the spheroid surface is located by its usual angles $\theta \in [0, 2\pi]$ and $\varphi \in [0, \pi]$ such that $x_1 = a\sin\varphi\cos\theta, x_2 = a\sin\varphi\sin\theta, x_3 = \lambda a\cos\varphi$ and for two positive integers $N_\varphi \geq 3$ and $E \geq 0$ we introduce the two-parameter mesh on S consisting of the nodal points $M = (\theta, \varphi) = (n_\theta, n_\varphi)$ such that

$$\begin{aligned} &\theta = 2\pi(n_\theta - 1)/N_\theta, \\ &\varphi = \pi n_\varphi/[2N_\varphi], \\ &N_\theta = 12 \times 2^E \end{aligned} \tag{75}$$

for positive integers n_θ and n_φ subject to the following conditions

$$1 \leq n_\theta \leq N_\theta \text{ if } 2 \leq n_\varphi \leq 2[N_\varphi - 1], \tag{76}$$

$$n_\theta = 2k,\ k = 0, \ldots, \frac{N_\theta}{2} - 1 \text{ if } 1 \leq n_\varphi \leq 2N_\varphi - 1. \tag{77}$$

One thus ends up with a $N-$node mesh of $N = 2[N_\theta + 1][N_\varphi - 1]$ collocation points and for conciseness we shall note $N = [N_\varphi, E]$. As previously pointed out, the accuracy of the advocated strategy (consisting of equations (61)-(65)) to compute $\phi, \phi_{,m}$ and $\nabla(\phi_{,m}).\mathbf{n}$ on the surface has been carefully checked in Sellier (2003b). In the present work the numerical treatment of the boundary-integral equations (56) and (60) has been also nicely tested against the analytical solutions (27)-(28) and (31)-(33) respectively by resorting to the above-mentioned $N-$node mesh.

As shown in Tab. 1, the computed coefficient $c(\delta)$ (recall (36)) for a conducting sphere ($\lambda = 1$) clearly converges towards its theoretical value as the number N of collocation points increases. A 4-digit accuracy is obtained and the magnitude of the computed angular velocity is of order 10^{-4} for the refined $1058-$node mesh whatever the value of the sphere relative conductivity δ.

For non-spherical spheroids it is sufficient to compare each computed coefficient c_k to its theoretical value (see (48)-(49)). Tab. 2 provides such comparisons both for oblate and prolate insulating or conducting spheroids. Again, an excellent agreement is found between the numerics and the theory. The magnitude of the computed angular velocity is of order 10^{-4} and a 4-digit accuracy is obtained for enough collocation points ($N = 1058$ or $N = 2210$ for the oblate and prolate spheroids, respectively).

Finally, we numerically check that a non-spherical spheroid may become motionless in

Table 1: Effect of mesh refinement for the computed coefficient $c(\delta)$, introduced by (36), for a conducting sphere. Computations have been performed for $(\mathbf{E},\mathbf{B}) = (E\mathbf{e}_3, B\mathbf{e}_1)$ and three numbers N of collocation points: $N = 72 = [4,0], N = 242 = [6,1]$ and $N = 1058 = [12,2]$.

N	$\delta = 0$	$\delta = 0.5$	$\delta = 2$	$\delta = 5$
74	-0.17447	-0.07025	0.08968	0.21399
242	-0.16756	-0.06704	0.08383	0.19169
1058	-0.16677	-0.06669	0.08335	0.19048
exact	-0.16667	-0.06667	0.08333	0.19048

Table 2: Computed coefficients c_k for a conducting oblate ($\lambda = 0.5$) or prolate ($\lambda = 2$) spheroid of relative conductivity δ and shape parameter λ. Refined meshes of $N = [12,2] = 1058$ or $N = [24,2] = 2210$ collocation points have been used for $\lambda = 0.5$ or $\lambda = 2$ respectively and the selected ambient electric and magnetic fields are $(\mathbf{E},\mathbf{B}) = (E\mathbf{e}_2, B\mathbf{e}_3)$ if $k = 1$, $(\mathbf{E},\mathbf{B}) = (E\mathbf{e}_3, B\mathbf{e}_1)$ if $k = 2$ and $(\mathbf{E},\mathbf{B}) = (E\mathbf{e}_1, B\mathbf{e}_2)$ if $k = 3$.

δ	λ	k	c_k : computed	c_k : exact
0	0.5	1	-0.10330	-0.10320
0	0.5	2	-0.13018	-0.12979
0	0.5	3	-0.08046	-0.08036
2	0.5	1	0.06381	0.06373
2	0.5	2	0.04030	0.04018
2	0.5	3	0.04971	0.04963
0	2	1	-0.23484	-0.23474
0	2	2	-0.22333	-0.22334
0	2	3	-0.31466	-0.31456
2	2	1	0.09751	0.09747
2	2	2	0.15727	0.15728
2	2	3	0.13065	0.13061

Table 3: Computed normalized velocities u_2 and ω_2 of prolate and oblate conducting spheroids for the critical setting $\mathbf{E} = E(\mathbf{e}_1 + \mathbf{e}_3)/\sqrt{2}, \mathbf{B} = B(\sin\varphi\mathbf{e}_1 + \cos\varphi\mathbf{e}_3)$ with $\tan\varphi = c_1/c_2$ and $EB \neq 0$. A coarse N_1-node mesh and a refined N_2-node mesh are employed with $N_1 = [4,0] = 72, N_2 = [12,2] = 1058$ for $\lambda = 0.5$ and $N_1 = [8,0] = 170, N_2 = [24,2] = 2210$ for $\lambda = 2$. Other computed quantities u_1, u_3, ω_1 and ω_3 are smaller in magnitude than 10^{-7} for the refined N_2-node mesh and thus not given here.

δ	λ	$u_2(N_1)$	$u_2(N_2)$	$\omega_2(N_1)$	$\omega_2(N_2)$
0	0.5	0.003063	-0.000115	-0.000074	0.000007
0.5	0.5	0.001069	-0.000043	-0.000026	0.000003
2	0.5	-0.001019	0.000058	0.000023	-0.000004
5	0.5	-0.001817	0.000035	0.000028	-0.000008
0	2	0.005157	0.000052	-0.000267	0.000003
0.5	2	0.002163	0.000021	-0.000109	-0.000001
2	2	-0.003023	-0.000027	0.000123	0.000001
5	2	-0.008313	-0.000061	0.000194	0.000001

Case 4 for adequately selected electric and magnetic fields such that $\mathbf{E}\wedge\mathbf{B}\neq\mathbf{0}$, as predicted in §3.2. Here we take $\mathbf{E}=E(\mathbf{e}_1+\mathbf{e}_3)/\sqrt{2}$ and, by virtue of (55), select the magnetic field as $\mathbf{B}=B(\sin\varphi\mathbf{e}_1+\cos\varphi\mathbf{e}_3)$ with $\tan\varphi=c_1/c_2$ and $EB\neq 0$. Under these choices, the following normalized velocity components

$$u_i=\frac{\mu\mathbf{U}.\mathbf{e}_i}{\sigma a^2EB},\quad \omega_i=\frac{\mu\boldsymbol{\omega}.\mathbf{e}_i}{\sigma aEB} \tag{78}$$

vanish. Our numerical results, given in Tab. 3 for $\lambda=0.5,2$ and $\delta=0,0.5,2,5$ perfectly agree with this prediction.

5.2 Case of conducting tori

Let us consider, as illustrated in Fig. 8, a conducting torus of uniform conductivity $\sigma_s\geq 0$ whose surface S admits the equation $[(x_1^2+x_2^2)^{1/2}-R]^2+x_3^2=a^2$ with $R>a>0$. For this geometry $\mathbf{n}(\mathbf{x})$ and $C(\mathbf{x})$ read

$$\mathbf{n}(\mathbf{x})=\left[1-\frac{R}{\sqrt{x_1^2+x_2^2}}\right]\left[\frac{x_1}{a}\mathbf{e}_1+\frac{x_2}{a}\mathbf{e}_2\right]+\frac{x_3}{a}\mathbf{e}_3, \tag{79}$$

$$C(\mathbf{x})=\frac{1}{a}\left[2-\frac{R}{\sqrt{x_1^2+x_2^2}}\right]. \tag{80}$$

Since orthotropic, the torus does not rotate and because $(O,\mathbf{e}_3)$ is axis of symmetry the only non-zero coefficients S_{ijk} that govern its translational velocity $\mathbf{U}$ (recall (25)) are $S_{123}=-S_{213}=a^2c_1, S_{231}=-S_{132}=a^2c_2$ and $S_{312}=-S_{321}=a^2c_3$ with, for $k=1,2,3$,

$$c_k=c_k(\delta,\eta),\quad \delta=\frac{\sigma_s}{\sigma}\geq 0,\quad \eta=\frac{R}{a}>1. \tag{81}$$

As sketched in Fig. 8, a nodal point M on S is located by its angles φ and θ lying in $[0,2\pi]$ and the $N-$node mesh is obtained by dividing the latter segment into N_φ or N_θ equal subdomains for φ and θ, respectively. All numerical computations are performed with $N_\varphi=20$ and $N_\theta=\eta N_\varphi$, a choice that is found to ascertain a sufficient $3-$digit accuracy for any computed coefficient c_k. Four geometries are addressed: $\eta=1.5,2,3,5$

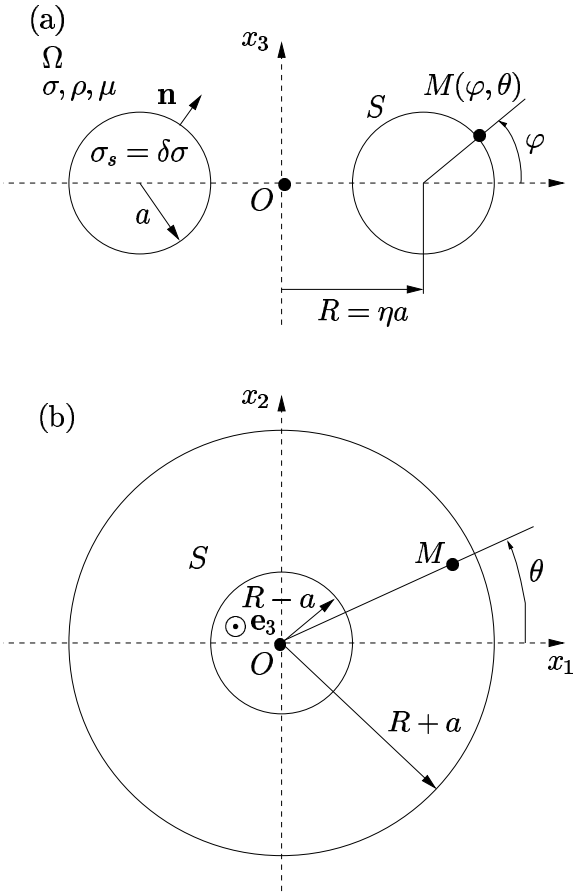

Figure 8: Employed notations for a conducting torus of shape parameter $\eta=2$. (a) torus cross-section. (b) torus top view.

and we thus spread 600 and 2000 collocation points on the surface of the small ($\eta=1.5$) and big ($\eta=5$) torus, respectively. For clarity, the coefficients c_k are plotted versus the relative conductivity δ in Fig. 9(a) for these two tori only and the reader may immediately obtain the behaviour for the other shape parameters $\eta=2,3$ by inspecting Fig. 9(c)-9(d).

As illustrated in Fig. 9(a) for $\eta=1.5$ and $\eta=5$, the translational velocity $\mathbf{U}$ of any conducting torus has been found to increase in magnitude with $|\delta-1|$ and to admit its smallest or biggest value in Cases 1 or 2 respectively for any given relative conductivity $\delta\geq 0$. Note that $|c_k|$ also increases with η but so does the torus volume $\mathscr{V}_{\mathscr{D}}=2\pi^2\eta a^3$. Accordingly, we also introduce

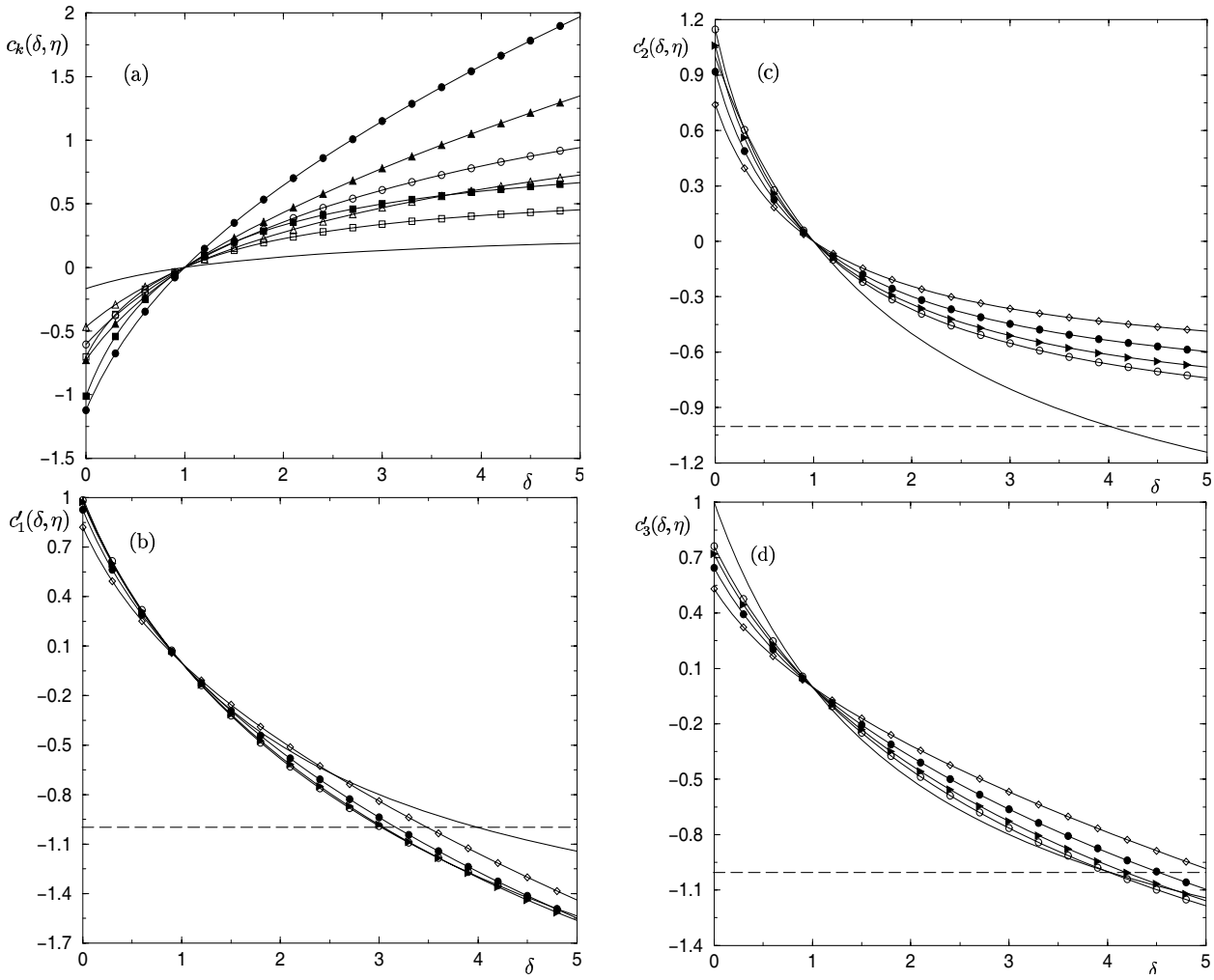

Figure 9: (a) Coefficients $c_k(\delta,\eta)$ for the small $(\eta = 1.5)$ and the big $(\eta = 5)$ tori in Case 1 ($\circ$ for $\eta = 1.5$ and $\bullet$ for $\eta = 5$), Case 2 ($\square$ for $\eta = 1.5$ and $\blacksquare$ for $\eta = 5$) and Case 3 ($\triangle$ for $\lambda = 1.5$ and $\blacktriangle$ for $\eta = 5$). (b)-(d) Normalized function c_k' for $\eta = 1.5(\circ), \eta = 2(\blacktriangleright), \eta = 3(\bullet)$ and $\eta = 5(\Diamond)$ in Cases 1 (b), 2 (c) and 3 (d). Below and above the horizontal long-dashed lines the torus translates faster than its volume equivalent insulating sphere. The case of the volume equivalent sphere of relative conductivity $\mathscr{S}_{ve}(\delta)$ is indicated by the solid curve.

the normalized coefficient c_k' which compares in Case k the torus velocity to the velocity of its volume equivalent insulating sphere $\mathscr{S}_{ve}(0)$, i. e. such that

$$c_k'(\delta,\eta) = -6c_k(\delta,\eta)[3\pi\eta/2]^{-2/3}. \tag{82}$$

The functions c_k' are plotted in Fig. 9(b)-9(d) which are the counter-parts of Fig. 4(a)-4(b). In each Case k, the torus migrates slower or faster than its volume equivalent *insulating* sphere $\mathscr{S}_{ve}(0)$ below or above the long-dashed horizontal line and the behavior of the volume equivalent sphere *of the same conductivity ratio* $\mathscr{S}_{ve}(\delta)$ is recalled by the solid curve. The coefficient c_1' is seen to weakly depend upon the shape-parameter η for $\delta \leq 1$. Each coefficient c_k' is seen to decrease in magnitude as η increases for any relative conductivity $\delta \geq 0$ whereas, depending upon both the selected Case k and the parameters (δ,η), the torus moves either slower or faster than its volume equivalent sphere $\mathscr{S}_{ve}(\delta)$. More precisely, the torus behaves like oblate spheroids (recall Fig. 4a) in Case 2 for $\delta \geq 1$ and Cases 1 or 3 for $\delta \leq 1$, i.e. it moves slower that $\mathscr{S}_{ve}(\delta)$. In other

instances, the torus adopts a prolate-like or oblate-like behavior depending on its shape parameter η only. For example, if it essentially moves faster or slower that $\mathscr{S}_{ve}(\delta)$ in Cases 1 and 3 respectively for $\delta \geq 1$ (as oblate spheroids do) it however migrates for $\delta \leq 1$ and Case 2 faster than $\mathscr{S}_{ve}(\delta)$ if $\eta \leq 2$ (oblate-like behavior) but slower than $\mathscr{S}_{ve}(\delta)$ if $\eta \geq 3$ (prolate-like behavior).

5.3 Case of conducting pear-shaped particles

As predicted in Moffatt and Sellier (2002) for $\delta = 0$ but also easily obtained by the same arguments for $\delta > 0$, any non-orthotropic and axisymmetric particle may both translate *and* rotate. Henceforth, we consider a particle that has length scale a and an axis of symmetry $(O,\mathbf{e})$ aligned with the unit vector $\mathbf{e}$. Adopting a frame of reference $(O,\mathbf{e}_1,\mathbf{e}_2,\mathbf{e}_3)$ such that $\mathbf{e}_3 = \mathbf{e}$, it is straightforward to establish that the particle rigid-body motion $(\mathbf{U},\boldsymbol{\omega})$ depends solely upon seven coefficients c_1,c_2,c_3 and r_1,r_2,r_3,r_4 as follows

$$U_1 = \frac{\sigma a^2}{\mu}\big\{c_1(\mathbf{E}.\mathbf{e}_2)(\mathbf{B}.\mathbf{e}_3) - c_2(\mathbf{E}.\mathbf{e}_3)(\mathbf{B}.\mathbf{e}_2)\big\}, \tag{83}$$

$$U_2 = \frac{\sigma a^2}{\mu}\big\{-c_1(\mathbf{E}.\mathbf{e}_1)(\mathbf{B}.\mathbf{e}_3) + c_2(\mathbf{E}.\mathbf{e}_3)(\mathbf{B}.\mathbf{e}_1)\big\}, \tag{84}$$

$$U_3 = \frac{\sigma a^2}{\mu}c_3(\mathbf{E}\wedge\mathbf{B}).\mathbf{e}_3, \tag{85}$$

$$\Omega_1 = \frac{\sigma a}{\mu}\big\{r_1(\mathbf{E}.\mathbf{e}_3)(\mathbf{B}.\mathbf{e}_1) + r_2(\mathbf{E}.\mathbf{e}_1)(\mathbf{B}.\mathbf{e}_3)\big\}, \tag{86}$$

$$\Omega_2 = \frac{\sigma a}{\mu}\big\{r_1(\mathbf{E}.\mathbf{e}_3)(\mathbf{B}.\mathbf{e}_2) + r_2(\mathbf{E}.\mathbf{e}_2)(\mathbf{B}.\mathbf{e}_3)\big\}, \tag{87}$$

$$\Omega_3 = \frac{\sigma a}{\mu}\big\{r_3(\mathbf{E}.\mathbf{e}_3)(\mathbf{B}.\mathbf{e}_3) + r_4[(\mathbf{E}.\mathbf{e}_1)(\mathbf{B}.\mathbf{e}_1) + (\mathbf{E}.\mathbf{e}_2)(\mathbf{B}.\mathbf{e}_2)]\big\}. \tag{88}$$

Each above coefficient c_k or r_l is determined by the particle geometry and relative conductivity $\delta \geq 0$ (of course c_k depends upon the point O attached to the particle and all coefficients r_l vanish when the body is orthotropic). From (83)-(85) it appears that relation (53) actually takes place as soon as the particle is only axisymmetric (and not necessarily orthotropic). Accordingly, one may successively obtain the coefficients c_1,c_2 and c_3 by addressing Cases 1, 2 and 3 (recall definitions (50)-(52)). By virtue of (86)-(88), the particle in general also rotates and therefore experiences a time-dependent rigid-body motion because its orientation (i. e. the orientation of the unit vector $\mathbf{e}$) relative to the steady ambient electric and magnetic fields $\mathbf{E}$ and $\mathbf{B}$ then evolves with time. Four different settings $(\mathbf{E},\mathbf{B})$ actually permit us to separately extract the coefficients $r_1,\ldots,r_4$. For instance, (86)-(88) immediately yield

$$\mathbf{U} = \mathbf{0},\ \boldsymbol{\omega} = \frac{\sigma a r_3}{\mu}[\mathbf{E}.\mathbf{B}]\mathbf{e} \ \text{ if } \ \mathbf{E}||\mathbf{e} \text{ and } \mathbf{B}||\mathbf{e}, \tag{89}$$

$$\mathbf{U} = \frac{\sigma a^2 c_3 \mathbf{E}}{\mu}\wedge\mathbf{B}, \quad \boldsymbol{\omega} = \frac{\sigma a r_4 \mathbf{E}.\mathbf{B}}{\mu}\mathbf{e} \quad \text{if } \ \mathbf{E}.\mathbf{e} = \mathbf{B}.\mathbf{e} = 0. \tag{90}$$

In the above circumstances, the rigid-body motion is steady: the vector $\mathbf{e}$ does not evolve with time and the particle rotates at a constant angular velocity about its axis of symmetry $(O,\mathbf{e})$ (it may also experience a translation parallel to $\mathbf{e}$). In addition, we see that if $\mathbf{E}.\mathbf{e} = \mathbf{E}.\mathbf{B} = 0$ then

$$\mathbf{U} = \frac{\sigma a^2 c_1}{\mu}\left\{\mathbf{E}\wedge\mathbf{B} + (\frac{c_3}{c_1} - 1)[(\mathbf{E}\wedge\mathbf{B}).\mathbf{e}]\mathbf{e}\right\}, \tag{91}$$

$$\boldsymbol{\omega} = \frac{\sigma a r_2}{\mu}(\mathbf{B}.\mathbf{e})\mathbf{E}, \tag{92}$$

whilst for $\mathbf{E}||\mathbf{e}$ and $\mathbf{B}.\mathbf{E} = 0$ one obtains

$$\mathbf{U} = \frac{\sigma a^2 c_2}{\mu}[\mathbf{E}\wedge\mathbf{B}], \quad \boldsymbol{\omega} = \frac{\sigma a r_1}{\mu}[\mathbf{E}.\mathbf{e}]\mathbf{B}. \tag{93}$$

If initial conditions (given by the initial value $\mathbf{e}(t_0)$ and the steady setting $(\mathbf{E},\mathbf{B})$) now fall into one of the above circumstances, the induced particle rigid-body motion clearly becomes time-dependent. More precisely, if $\mathbf{E}.\mathbf{B} = \mathbf{E}.\mathbf{e}(t_0) = 0$ the particle translates and keeps rotating about the axis $(O,\mathbf{E})$ with $(\mathbf{U},\boldsymbol{\omega})$ given by (91)-(92) where $\mathbf{e} = \mathbf{e}(t)$. Of course, it will then stop rotating as soon as its axis of symmetry $(O,\mathbf{e})$ becomes normal to the magnetic field $\mathbf{B}$. If $\mathbf{E}.\mathbf{B} = 0$ and $\mathbf{E}$ is

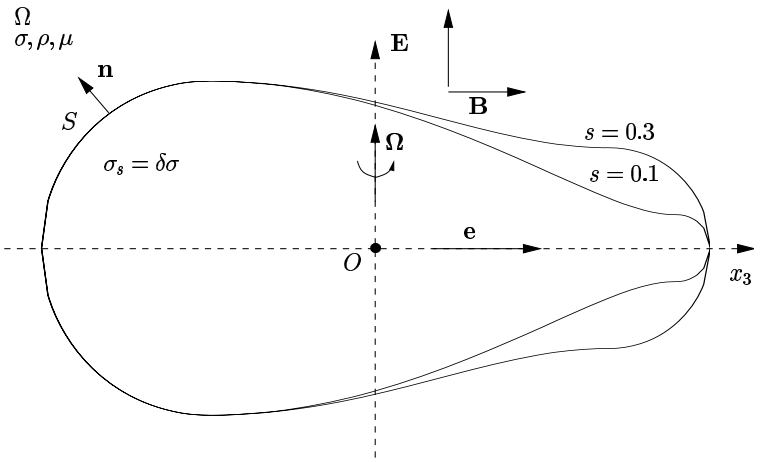

Figure 10: Selected conducting pear-shaped particles for $s = 0.1$ and $s = 0.3$. The frame of reference $(O, \mathbf{e}_1, \mathbf{e}_2, \mathbf{e}_3)$ is such that $\mathbf{e} = \mathbf{e}_3$ and the rigid-body motion $(\mathbf{U}, \blacksquare)$ is given by (93).

Table 4: Computed coefficients c_1 and r_2 for two insulating or conducting pear-sphaped particles of shape-parameters $s = 0.1$ and $s = 0.3$ Three increasing numbers N of collocation points are employed: $N_1 = [10,0] = 218, N_2 = [20,1] = 914$ and $N_3 = [40,1] = 1874$.

s	δ	$c_1(N_1)$	$c_2(N_2)$	$c_1(N_3)$	$r_2(N_1)$	$r_2(N_2)$	$r_2(N_3)$
0.1	0.	-0.04627	-0.04727	-0.04724	0.01031	0.01036	0.01036
0.3	0.	-0.05108	-0.05235	-0.05234	0.00720	0.00727	0.00726
0.1	5.	0.04310	0.04343	0.04333	-0.01505	-0.01360	-0.01367
0.3	5.	0.04586	0.04660	0.04652	-0.01213	-0.01050	-0.01053
0.1	10.	0.05560	0.05552	0.05524	-0.02131	-0.01787	-0.01804
0.3	10.	0.05865	0.05930	0.05909	-0.01789	-0.01393	-0.01399

aligned with $\mathbf{e}(t_0)$ the particle this time starts rotating about the axis $(O, \mathbf{B})$ and the orientation of $\mathbf{e}(t)$ relative to $\mathbf{E}$ therefore changes. However, if one denotes by B and $\mathbf{e}'$ the magnitude of $\mathbf{B}$ and the unit vector $\mathbf{e}' = \mathbf{B} \wedge \mathbf{e}/B$, observe that $\mathbf{E} = (\mathbf{E}.\mathbf{e})\mathbf{e} + (\mathbf{E}.\mathbf{e}')\mathbf{e}'$ at any time t with $\mathbf{e}'.\mathbf{B} = 0$. By virtue of (90) and (92), the unsteady rigid-body motion $(\mathbf{U}, \boldsymbol{\omega})$ then reads

$$\mathbf{U} = \frac{\sigma a^2}{\mu}\big\{c_2(\mathbf{E}.\mathbf{e})\mathbf{e} \wedge \mathbf{B} + c_3[\mathbf{E}.(\mathbf{B} \wedge \mathbf{e})]\mathbf{e}\big\}, \quad (94)$$

$$\boldsymbol{\omega} = \frac{\sigma a r_1}{\mu}[\mathbf{E}.\mathbf{e}]\mathbf{B} \quad (95)$$

with of course $\mathbf{e} = \mathbf{e}(t)$. Accordingly, the particles rotates about the axis $(O, \mathbf{B})$ at any time and stop rotating as soon as $\mathbf{e}(t)$ becomes this time normal to the electric field $\mathbf{E}$.

Circumstances (93) are illustrated in Fig. 10 for a conducting pear-shaped particle. The surface S admits, for Cartesian coordinates (O, x_1, x_2, x_3) such that $\mathbf{e}_3 = \mathbf{e}$, the equation $\{x_1^2 + x_2^2\}^{1/2} = a h_s(x_3/a)$ where $|x_3/a| \leq 1$ and the positive profile function h_s is defined versus the shape parameter $0 < s < 1$ in Appendix C. Henceforth, numerical results are given for the two sketched geometries ($s = 0.1$ and $s = 0.3$); two particles which are clearly far from being orthotropic. Any nodal point M on S is located by its angles $\theta \in [0, 2\pi]$ and $\varphi \in [0, \pi]$ such that $x_3 = a\cos\varphi, x_1 = a h_s(\cos\varphi)\cos\theta$ and $x_2 = a h_s(\cos\varphi)\sin\theta$ with the same discretization procedure in (θ, φ) as for spheroids (see (75)-77)).

All numerical computations employ $N = [20,1] = 914$ collocation points on the 'pear' surface; a choice that yields (see Tab. 4) a $4-$digit accuracy for coefficients c_k and r_l in the range $0 \leq \delta \leq 10$. As shown in Fig. 11(a), the translation $\mathbf{U}$ increases in magnitude with $|\delta - 1|$ and admits its smallest value in Case 1 and its biggest value in Case 2 if $\delta > 1$ (with $c_2 > c_3 > c_1 > 0$) and in

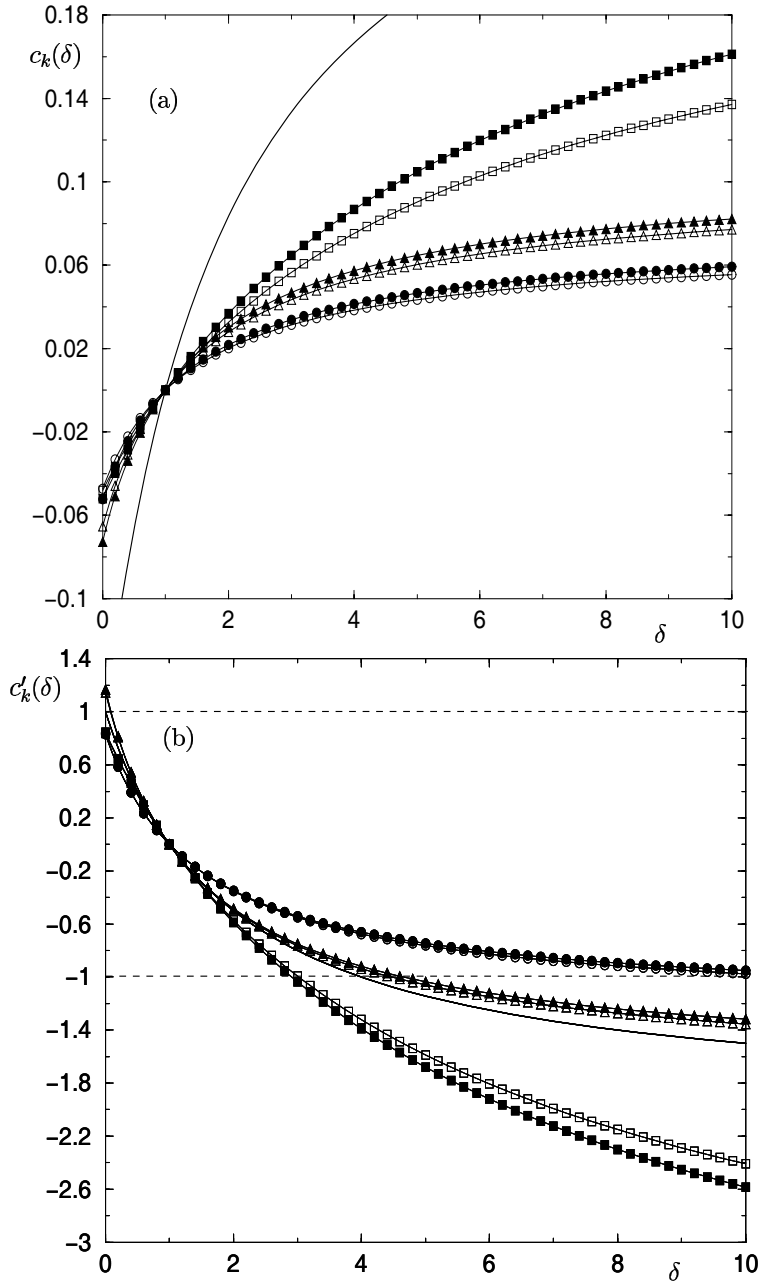

Figure 11: Coefficients c_k and c'_k for $s = 0.1$ (clear symbols) and $s = 0.3$ (filled symbols). (a) c_1 (circles), c_2 (squares) and c_3 (triangles). The coefficient $c(\delta)$ for a conducting sphere of radius a is recalled by the solid curve. (b) c'_1 (circles), c'_2 (squares) and c'_3 (triangles). Above and below horizontal long-dashed lines the particle moves faster and slower respectively than its volume equivalent insulating sphere $\mathscr{S}_{ve}(0)$. Solid curve: case of the volume equivalent conducting sphere $\mathscr{S}_{ve}(\delta)$.

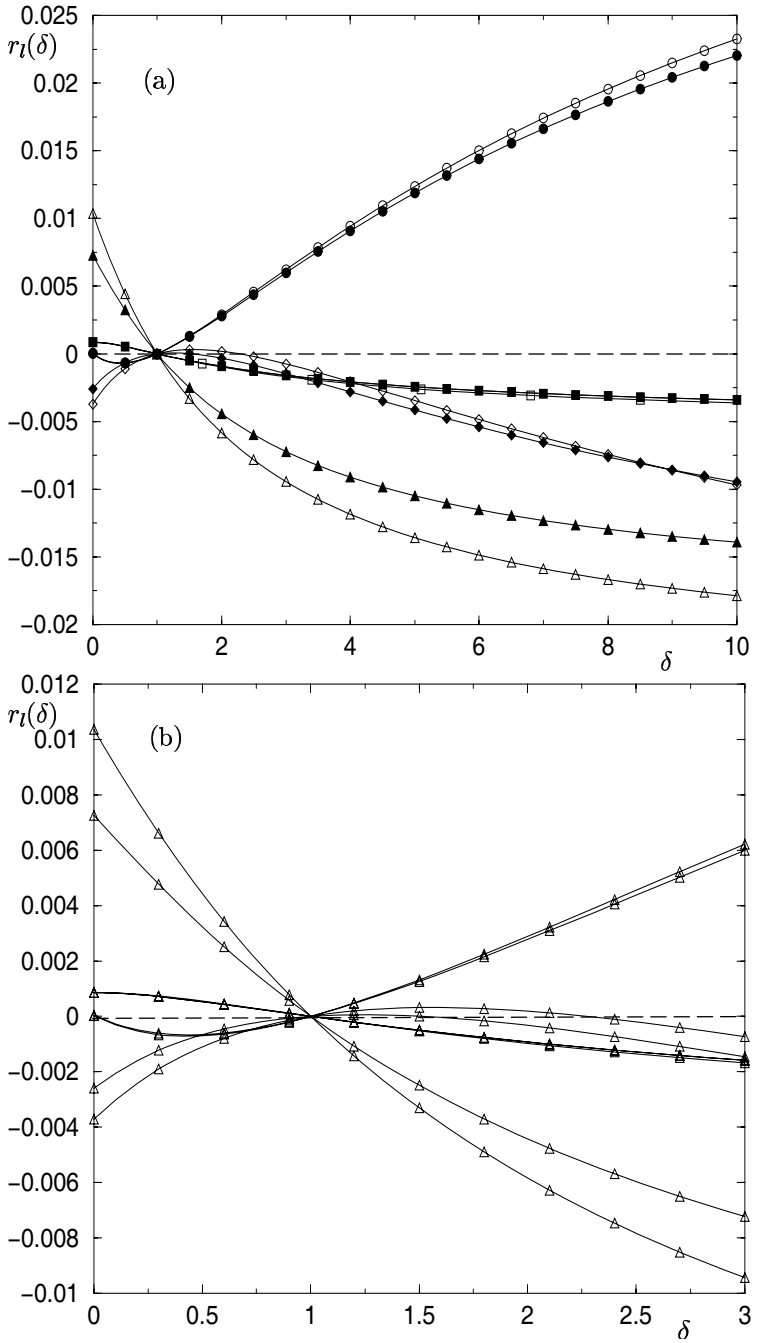

Figure 12: Coefficients r_1 (diamonds), r_2 (triangles), r_3 (circles) and r_4 (squares) for the shape parameters $s = 0.1$ (clear symbols) and $s = 0.3$ (filled symbols). (a) Case $0 \leq \delta \leq 10$. (b) Magnified figure for $0 \leq \delta \leq 3$.

Case 3 if $\delta < 1$ (with $c_3 < c_2 < c_1 < 0$).

Again, we introduce the coefficient c'_k, which compares in Case k the particle velocity to the velocity of the volume equivalent insulating sphere $\mathscr{S}_{ve}(0)$, as

$$c'_k = -6c_k \left[3\mathscr{V}_{\mathscr{P}}/(4\pi a^3)\right]^{-2/3} \tag{96}$$

with $\mathscr{V}_{\mathscr{P}}$ the particle volume. As revealed by Fig. 11(b), each pear-shaped particle not surprisingly behaves like prolate spheroids (see once more Fig. 4b): it moves faster than its volume equivalent sphere $\mathscr{S}_{ve}(\delta)$ of the same relative conductivity δ in Case 2 for $\delta > 1$ and Case 3 for $\delta < 1$ and slower than $\mathscr{S}_{ve}(\delta)$ otherwise.

Finally, the coefficients r_l are plotted in Fig. 12. Clearly, r_2 and r_4 have sign of $1-\delta$, increase in magnitude with $|\delta - 1|$ and depend on the shape parameter s. By contrast, r_1 and r_3 depend upon s and exhibit a more subtle behavior for $\delta > 1$ or $\delta < 1$ (see the magnified Fig. 12b): these coefficients not only vanish with $\delta = 1$ but also for $\delta \sim 2.2$ and $\delta = 0$, respectively.

6 Concluding remarks

A whole boundary-integral formulation and its numerical implementation have been proposed to accurately compute at a reasonable cpu cost the rigid-body motion of a conducting and arbitrarily-shaped particle subject to uniform ambient fields **E** and **B**. The translation of a conducting ellipsoid is analytically obtained and the accuracy of the advocated procedure is then demonstrated by the nice agreement, for spheroids, between the numerics and the theory. It is shown that two similar ellipsoids (admitting the same planes of symmetry but different in size) may become 'equivalent' for adequately selected conductivities, i. e. experience the same translation whatever the magnetic field **B** for a prescribed electric field **E** normal to a plane of symmetry. In addition to spheroids, the behavior of conducting tori and pear-shaped particles is numerically investigated. The translational velocity **U** of these axisymmetric bodies is found to deeply depend upon $(\mathbf{E},\mathbf{B})$, the particle shape and its relative conductivity δ. For instance, contrary to the case of spheres and as already pointed out for insulating spheroids in Sellier (2003a), **U** is in general not aligned with $\mathbf{E}\wedge\mathbf{B}$ and one can select $(\mathbf{E},\mathbf{B})$ so that **U** vanishes for $\delta \neq 1$ (recall Case 4, depicted in Fig. 3(d), and choose angles θ and φ such that $\tan\varphi = c_1 \tan\theta/c_2$). Among the considered geometries, only pear-shaped particles are non-orthotropic and rotate. The induced rigid-body motion thus becomes time-dependent and the angular velocity $\boldsymbol{\omega}$ is also greatly sensitive to δ, the particle shape and the uniform ambient fields **E** and **B**.

So far, particle-particle interactions have been neglected. However, the rigid-body motions of two close enough conducting particles might strongly differ from the values predicted by the present study. In future it would thus be nice to extend the proposed procedure to the case of a N-particle cluster with $N \geq 2$. Such a challenging issue is under current investigation.

References

Beskos, D. E. (1987): Introduction to Boundary Element Methods. In *Computational Methods in Mechanics* (ed. D. E. Beskos). Elsevier Science Publishers.

Bonnet, M. (1999): *Boundary Integral Equation Methods for Solids and Fluids*. John Wiley & Sons Ltd.

Brebbia, C. A.; Telles J. C. L.; Wrobel, L. C. (1984): *Boundary Element Techniques*. Springer-Verlag, Theory and Applications in Engineering, Berlin Heidelberg New York Tokyo.

Duddeck, F. (2006): An Alternative Approach to Boundary Element Methods via the Fourier Transform. *CMES: Computer Modeling in Engineering & Sciences*, **15**, 1, 1–14.

Duduchava, R. (2001): The Green formula and layer potentials. *Integral Equations and Operatot Theory.* **41**, 127–178.

Gardano, P.; Dabnichki, P. (2006): Application of Boundary Element Method to Modelling of Added Mass and Its Effect on Hydrodynamic Forces. *CMES: Computer Modeling in Engineering & Sciences*, **15**, 2, 87–98.

Gradshteyn, I. S.; Ryzhik, I. M. (1965): *Tables of integrals, Series and Products*. Academic Press.

Happel, J.; Brenner, H. (1973): *Low Reynolds Number Hydrodynamics*. Martinus Nijhoff.

Hsiao, S. -C.; and Ingber, M. S. (2004): The Effect of the Reynolds Number on Lateral Migration of Nonneutrally-Buoyant Spherical Particles in Poiseuille Flow. *CMC: Computers, Materials & Continua*, **1**, 1, 51–58.

Jackson, J. D. (1975): *Classical Electrodynamics*. New York: Wiley.

Jeffery, G. B. (1922): The motion of ellipsoidal particles immersed in a viscous fluid. *Proc. Roy. Soc. Lond. A*. **102**, 161–179.

Kim, S.; Karrila, S. J. (1991): *Microhydrodynamics: Principles and Selected Applications*. Butterworth.

Kolin, A. (1953): An electromagnetokinetic phenomenon involving migration of neutral particles. *Science*, **117**, 134–137.

Leenov, D.; Kolin, A. (1954): Theory of electromagnetophoresis. I. Magnetohydrodynamic forces experienced by spherical and symmetrically oriented cylindrical particles. *J.Chem.Phys.*, **22**, 683–688.

Ladyzhenskaya, O. A. (1969): *The Mathematical Theory of Vicous Incompressible Flow*. Gordon & Breach.

Lamb, H. (1932): *Hydrodynamics*. 6th edn, Cambridge University Press.

Lyness, J. N.; Jespersen, D. (1975): Moderate Degree Symmetric Quadrature Rules for the Triangle. *J. Inst. Maths. Applics*, **15**, 19–32.

Marty, P.; Alemany, A. (1984): Theoretical and experimental aspects of electromagnetic separation. In *Metallurgical Applications of Magnetohydrodynamics*, (ed. H.K.Moffatt & M.R.E. Proctor). Metals Society, pp. 245–259.

Moffatt, H. K.; Sellier, A. (2002): Migration of an insulating particle under the action of uniform ambient electric and magnetic fields. Part 1. General theory. *J. Fluid Mech.* **464**, 279–286.

Pozrikidis, C. (1992): *Boundary integral and singularity methods for linearized viscous flow*. Cambridge University Press.

Rezayat, M.; Shippy, D. J.; Rizzo, F. J. (1986): On time-harmonic elastic-wave analysis by the Boundary Element Method for moderate to high frequencies. *Comp. Meth. in Appl. Mech. Engng.* **55**, 349–367.

Sanz, J. A.; Solis, M.; Dominguez J. (2007): Hypersingular BEM for Piezoelectric Solids: Formulation and Applications for Fracture Mechanics. *CMES: Computer Modeling in Engineering & Sciences*, **17**, 3, 215–230.

Sellier, A. (2003a): Migration of an insulating particle under the action of uniform ambient electric and magnetic fields. Part 2. Boundary formulation and ellipsoidal particles. *to appear in J. Fluid Mech.*

Sellier, A. (2003b): On the numerical approximation of the derivatives of potentials on the smooth and simply or multiply connected boundary by using boundary-integral equations. *Submitted to Proc. R. Soc. Lond. A.*

Sellier, A.; Pasol, L. (2006): Sedimentation of a Solid Particle Immersed in a Fluid Film. *CMES: Computer Modeling in Engineering & Sciences*, **16**, 3, 187–196.

Trang-Cong, T.; Phan-Thien, N. (1989): Stokes problems of multiparticle systems: A numerical method for arbitrary flows. *Phys. Fluids. A.***1**, 3, 453-461.

Zabreyko, R. P. (1975): *Integral equations*. Leyden: Noordhoff.

Appendix A:

This Appendix shows that the particle of relative conductivity $\delta = \sigma_s/\sigma \geq 0$ is electrically neutral

and establishes the results (21)-(22) for the vector

$$\mathbf{A}=\int_{\mathscr{P}}\mathbf{a}(\mathbf{x})dv,\quad \mathbf{a}(\mathbf{x})=\mathbf{x}\wedge[\nabla\phi'\wedge\mathbf{B}]=a_i(\mathbf{x})\mathbf{e}_i. \tag{97}$$

From (18) it is clear that $q=0$ if $\delta=1$. If $\delta\neq 1$, the integration of (18) over the surface S for $\mathbf{E}$ uniform and $\nabla^2\phi'=0$ inside the particle also yields

$$\int_S q(\mathbf{x})dS=(\delta-1)\int_S \mathbf{E}.\mathbf{n}dS=0. \tag{98}$$

Appealing to the usual relation $\mathbf{b}\wedge(\mathbf{c}\wedge\mathbf{d})=(\mathbf{b}.\mathbf{d})\mathbf{c}-(\mathbf{b}.\mathbf{c})\mathbf{d}$ and a few elementary algebra, the reader may easily check that for $\mathbf{B}$ *uniform*

$$\begin{aligned}a_i(\mathbf{x})&=(\mathbf{B}.\mathbf{x})(\nabla\phi'.\mathbf{e}_i)-(\mathbf{B}.\mathbf{e}_i)(\nabla\phi'.\mathbf{x})\\&=\nabla.\left\{\phi'[(\mathbf{B}.\mathbf{x})\mathbf{e}_i-(\mathbf{B}.\mathbf{e}_i)\mathbf{x}]\right\}+2\phi'(\mathbf{x})\mathbf{B}.\mathbf{e}_i.\end{aligned} \tag{99}$$

Accordingly, we immediately arrive at

$$\begin{aligned}\mathbf{A}.\mathbf{e}_i=&\int_S\phi'(\mathbf{x})\left[(\mathbf{B}.\mathbf{x})\mathbf{e}_i-(\mathbf{B}.\mathbf{e}_i)\mathbf{x}\right].\mathbf{n}dS\\&+2(\mathbf{B}.\mathbf{e}_i)\int_{\mathscr{P}}\phi'(\mathbf{x})dv.\end{aligned} \tag{100}$$

The volume integral on the right-hand side of (100) is treated by appealing to the single-layer representation (16) of ϕ' in the domain $\mathscr{P}$. Noting that for $\mathbf{OP}=\mathbf{y}=y_i\mathbf{e}_i$ the simple relation $2/MP=\partial[\mathbf{MP}.\mathbf{e}_i/MP]/\partial y_i=\nabla_{\mathbf{y}}.(\mathbf{MP}/MP)$ holds, the result reads

$$\begin{aligned}4\pi\int_{\mathscr{P}}\phi'(\mathbf{y})dv&=\int_S q(M)\left[\int_{\mathscr{P}}\frac{dv}{PM}\right]dS_M\\&=\frac{1}{2}\int_S q(M)\left[\int_S\frac{\mathbf{MP}.\mathbf{n}(P)}{MP}dS_P\right]dS_M.\end{aligned} \tag{101}$$

Since $\phi'=\phi$ on S we thus deduce (21)-(22) from (100)-(101).

Appendix B:

This Appendix establishes the results (31)-(33) when $\mathbf{E}=E\mathbf{e}_2$. Following Lamb (1932) (see §111 − 114) we select the perturbation potentials ϕ' and ϕ as

$$\phi'(\mathbf{x})=-\frac{AE\alpha_2 x_2}{a_1a_2a_3}\text{ in }\mathscr{P}, \tag{102}$$

$$\phi(\mathbf{x})=-AE\left[\int_{\lambda(\mathbf{x})}^{\infty}\frac{dt}{\gamma(t)(a_2^2+t)}\right]\text{ in }\Omega \tag{103}$$

with α_2 and the function γ defined as in (29)-(30), $\lambda(\mathbf{x})$ the greatest positive root of the equation $x_1^2/(a_1^2+\lambda)+x_2^2/(a_2^2+\lambda)+x_3^2/(a_3^2+\lambda)=1$ considered as cubic in λ and A a coefficient to be determined. Under these choices, ϕ' and ϕ are harmonic in $\mathscr{P}$ and Ω respectively and $\nabla\phi\to\mathbf{0}$ as $r\to 0$, i. e. (2) indeed holds. Noting that λ vanishes on the ellipsoid surface of equation (26), the definition (29) of α_2 also ensures that $\phi'=\phi$ on S. Thus, A is obtained from the boundary condition (3), i.e. $\delta(E\mathbf{e}_2-\nabla\phi').\mathbf{n}=(E\mathbf{e}_2-\nabla\phi).\mathbf{n}$ on S. Exploiting Lamb (1932) the relations (without summation over suffixes i in (104))

$$\left(\frac{\partial\lambda}{\partial x_i}\right)=\frac{2s^2(\mathbf{x})x_i}{a_i^2},\quad \mathbf{n}.\mathbf{e}_i=\frac{s(\mathbf{x})x_i}{a_i^2} \tag{104}$$

we immediately obtain, from (102)-(103),

$$\delta(E\mathbf{e}_2-\nabla\phi').\mathbf{n}=\delta E\left[1+\frac{A\alpha_2}{a_1a_2a_3}\right]\mathbf{e}_2.\mathbf{n}, \tag{105}$$

$$(E\mathbf{e}_2-\nabla\phi).\mathbf{n}=E\left[1+\frac{A(\alpha_2-2)}{a_1a_2a_3}\right]\mathbf{e}_2.\mathbf{n}. \tag{106}$$

Accordingly, the required coefficient A is found to be

$$A=\frac{a_1a_2a_3(1-\delta)}{2+(\delta-1)\alpha_2} \tag{107}$$

and using (17) to compute the associated polarization surface-charge density q we easily arrive at the announced results (31)-(33).

Appendix C:

In this Appendix we define the profile function h_s for the addressed pear-shaped particles (see §5.3) and also provide the associated normal vector $\mathbf{n}(\mathbf{x})$ and the mean curvature $C(\mathbf{x})$. For $0<s<1$ the selected function $v_s=h_s^2$ obeys

$$v_s(u)=-u(u+1)\text{ if }-1\leq u\leq-\frac{1}{2}, \tag{108}$$

$$v_s(u)=(1-u)(u-1+2s)\text{ if }1-s\leq u\leq 1, \tag{109}$$

$$v_s(u)=s^2+\frac{1-4s^2}{8}\left\{1-\right.$$

$$\sin\left[\frac{2\pi}{3-2s}\left(u+\frac{2s-1}{4}\right)\right]\Bigg\} \text{ if } -0.5 \le u \le 1-s. \tag{110}$$

By introducing the first-order and second-order derivatives $v_s^{(1)} = dv_s/du$ and $v_s^{(2)} = dv_s^{(1)}/du$ we thus arrive, after elementary algebra, at

$$\mathbf{n}(\mathbf{x}) = x_1\mathbf{e}_1 + x_2\mathbf{e}_2 - av_s^{(1)}(u)/2\mathbf{e}_3, \tag{111}$$

$$d = x_1^2 + x_2^2 + \left[av_s^{(1)}(u)/2\right]^2, \;\; u = x_3/a, \tag{112}$$

$$C(\mathbf{x}) = d^{-1/2}\Bigg\{2 - \frac{v_s^{(2)}(u)}{2} - \frac{1}{d}\left[x_1^2 + x_2^2 - a^2 v_s^{(1)}(u)v_s^{(1)}(u)v_s^{(2)}(u)/8\right]\Bigg\}. \tag{113}$$